Optical properties of aluminium clusters embedded in amorphous silicon and silicon nitride films

Abstract

Increasing the optical absorption of thin film solar cells is necessary to increase their efficiency and reduce material costs. Plasmonic scattering nanoparticles are a way to increase absorption in these cells. A lot of research on gold and silver plasmonic nanoparticles has been done, also in the context of solar cells, but these materials are expensive and alternatives are needed. In this thesis the optical properties of aluminium clusters embedded in silicon nitride and amorphous silicon were studied. The aluminium clusters embedded in silicon nitride and amorphous silicon were fabricated by a gas aggregation cluster source combined with a thin film magnetron sputtering source combined in a single vacuum system. The topography of the samples was studied using atomic force microscopy (AFM), while the optical properties of the samples were studied using UV-Vis optical absorption spectroscopy. Finite difference time domain (FDTD) simulations were performed to calculate the optical absorption and the extinction cross section of the cluster-thin-film composites. Aluminium particles with a typical radius of 4-8 nm and a density between 10 and 20 clusters per square micron were made, which were covered with the thin films. Enhanced optical absorption near the red-shifted plasmon frequency in silicon nitride was observed, which was in agreement with the FDTD simulations. Although the FDTD simulations predicted a resonance well matched to the solar spectrum with the amorphous silicon film, no clear plasmon resonance was observed at the expected wavelength. However, a significant difference in optical absorption at wavelengths below 400 nm was observed in the samples with aluminium clusters covered with a 25 nm film of amorphous silicon. Both with silicon nitride and amorphous silicon, the aluminium clusters increased optical absorption.

Thomas van der Vliet
Natural Science Project
February 2013 - October 2014
Debye institute
Supervised by dr. Marcel Di Vece

Contents

Introduction (1)

Solar photovoltaics (PV) is a technology to produce renewable electricity directly from the solar radiation that reaches the earth. Over the past few decades it has evolved from a niche product used in satellites and buoys to a small but significant source of electric power in the world. The most widely used PV panels use polycrystalline silicon cells. Commercial c-Si cells have a typical efficiency between 15 and 20%. Prices have decreased rapidly and steadily of the past years, the technology is maturing and prices are dropping through technological learning and economies of scale more than big scientific breakthroughs.

There are alternatives to c-Si solar cells, such as thin film solar cells and organic solar cells. Thin film solar cells have a thickness of +- 250 nm versus a typical thickness of 200 µm for c-Si cells. This is because crystalline silicon has an indirect bandgap, which means that there is a momentum mismatch between the incident photon and an electron-hole pair that is generated. The momentum mismatch is compensated by a phonon. This makes carrier generation a three particle interaction, which is less likely to occur than a two particle interaction. Therefore the absorption of light in c-Si is relatively poor.

The thin film technologies do not have this disadvantage. The main thin film technologies are Cadmium Telluride and hydrogenated amorphous silicon solar cells (CdTe and a-Si:H). Cadmium Telluride has a bandgap of 1.4 eV, which is near perfect for a single junction solar cell according to the Shockley-Queisser limit, which states that the maximum efficiency for a single junction solar cell is 33.7% at a bandgap of 1.34eV. CdTe has the disadvantage that Telluride is rare and Cadmium is toxic. For large scale applications the relative scarcity of Telluride compared to materials such as silicon is a problem.

Amorphous silicon (1.1)

Amorphous silicon has a direct bandgap of about 1.7 eV, which is above the ideal value for a single junction cell. The absorption of red and near infrared light is very poor for amorphous solar cells. This reduces the maximum efficiency compared with the Shockley-Quiesser limit. Typical a-Si:H cells do not nearly reach this efficiency, at 7 to 10%. This is because a-Si has many defects and dangling bonds; this decreases the efficiency significantly because of recombination. The thicker the absorbing layer, the higher these losses will be.

If a-Si:H cells could be made thinner while keeping the absorption of light constant the efficiency of the cell can be increased. Enhancing optical absorption is therefore key to making a-Si:H solar cells competitive. Conventional techniques for increasing optical path length used in c-Si cells use roughness at the front or rear of the cell to reflect incoming light. These structures are on the order of a micrometer in size, which is too large for thin film solar cells. Also, rough or jagged structures in an a-Si:H cell would increase the number of defects at the surface, further decreasing efficiency.

There are however unconventional techniques using features that are small enough for thin film cells that can be used to enhance optical absorption. The field of plasmonics has generated a lot of potential ways to increase absorption using localized surface plasmons, or propagating surface plasmon polaritons.

Plasmonics (1.2)

A plasmon is a collective oscillation of electrons in matter; these can occur in bulk (volume plasmon) or at the surface of a metal (surface plasmon). Volume plasmons can be created by the impact of a charged particle such as an electron. Surface plasmons can be created by incident electromagnetic radiation, they strongly enhance the local field and can act as scattering centres. This is why surface plasmons have potential applications in solar PV. The incoming radiation causes a surface plasmon resonance in a metal and the metal scatters the radiation and increases the near field. This could increase optical absorption in solar cells.

Three main configurations for using plasmons in solar cells have been proposed (Atwater&Polman, 2013):

- Forward scattering, where the strong scattering of metal nanoparticles is used to increase the path length of the incoming light and to trap it. In metal nanoparticles the field is localized, such a plasmon is called a localized surface plasmon (LSP).
- Near-field enhancement, where the particles are embedded in the absorbing layer. The strongly enhanced field around the particle increases absorption.
- Grating, where the light that reaches the end of the cell is coupled into a propagating surface plasmon polariton (SPP). The grating is needed because there is a momentum mismatch between the propagating wave and the incident radiation.

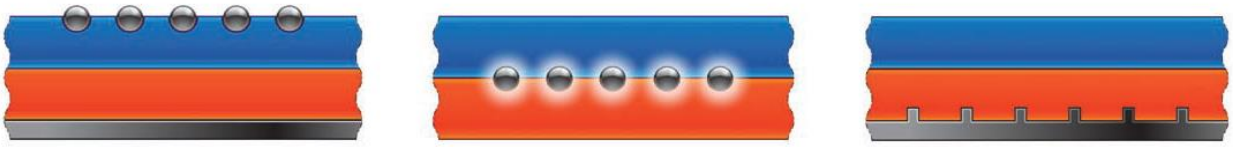

Figure 1. Left to right: scattering configuration, near-field enhancement configuration and grating configuration. Image taken from (Atwater&Polman, 2013)

In this research we focused on the scattering configuration. Earlier research on metal nanoclusters for scattering and increased absorption has mostly been with silver and gold clusters. While silver and gold exhibit strong resonances in the optical part of the spectrum, they are expensive and gold suffers from strong interband transitions. Therefore we use aluminium nanoparticles. Aluminium nanoparticles in air have a resonance around 150 nm. However, this resonance can be shifted by embedding the nanoparticles in a dielectric[1]. This can shift the resonance towards 300 nm using silicon nitride; with amorphous silicon the resonance shifts to about 600 nm and becomes interesting for applications in a-Si:H solar cells.

[1] (Kreibig&Vollmer, 1995)

Previous research (1.3)

Important work on plasmonics for enhanced absorption or light trapping in solar cells has been done by Albert Polman, Harry Atwater, Nakayama[2] and Hägglund[3], among others. The metal particles or disks that are studied are often silver or gold. Since these materials are expensive, alternatives such as aluminium also require study. Relatively little research has been done on plasmonic aluminium nanoparticles, especially in the context of solar cells.

Important work on plasmonic aluminium nanoparticles has been done by Yuri A. Akimov and Wee Shing Koh, mostly through computer simulations, to study the effect of aluminium particle size and density on the optical absorption in thin film solar cells[4]. For aluminium nanoparticles with a radius of 20 nm and a surface coverage of 60% Akimov and Koh found that the absorption could be enhanced by almost 25% in a modeled solar cell with a 250 nm a-Si layer, compared with 15% maximum enhancement for silver nanoparticles. Akimov also found that oxidation had a large negative effect on the absorption for silver nanoparticles and a very limited effect on the performance of the aluminium nanoparticles. He also found that the higher order modes are more suited for enhancement of optical absorption in solar cells[5], which also favours aluminium over gold and silver because for these metals the dipole mode is in the optical range of the spectrum and the dipole mode has very high absorption compared to its scattering. The high losses in metals such as copper, silver and gold due to interband transitions make the Mie resonances of materials such as TiO_2 perhaps even more interesting towards enhancement of optical absorption than the plasmon resonance of these metals, according to Akimov[6].

Some notable experimental work on aluminium plasmonic nanoparticles has been done, for instance in printing (Tan, 2014), but also towards coupling of light into silicon layers (Villesen, 2012). Villesen produced aluminium nanodiscs with a diameter and height of 100 nm using electron beam lithography. They were able to increase the quantum efficiency for wavelengths above 465 nm using aluminium nanodiscs on a thin film solar cell, leading to an increase in photocurrent of 2.8%.

Experimental work on aluminium nanoparticles embedded in dielectrics to enhance optical absorption in thin film solar cells is limited compared with gold and silver nanoparticles. On the other hand, according to the numerical work of Akimov and Koh aluminium is potentially better than silver because there is less parasitic absorption of the dipole mode in the optical part of the spectrum and it suffers less from oxidation. The combination of promising numerical results and the lack of experimental work on aluminium nanoparticles for enhanced absorption makes this study on the optical properties of aluminium clusters embedded in silicon nitride and amorphous silicon relevant today.

[2] Plasmonic nanoparticle enhanced light absorption in GaAs solar cells (Nakayama, 2008)
[3] Electromagnetic coupling of light into a silicon solar cell by nanodisk plasmons (Hägglund, 2008)
[4] (Akimov&Koh, Resonant and nonresonant plasmonic nanoparticle enhancement for thin-film solar cells, 2010)
[5] Enhancement of optical absorption in thin film solar cells through the excitation of higher order nanoparticle plasmon modes (Akimov K. , 2009)
[6] Nanoparticle-enhanced thin film solar cells: Metallic or dielectric nanoparticles? (Akimov K. R., 2010)

Research outline (1.4)

In this research we studied aluminium nanoclusters embedded in silicon nitride and amorphous silicon deposited on glass. Clusters were created using the Oxford Applied Research NC-200UB nanocluster source, the silicon nitride and silicon layers were produced via magnetron sputtering.

First we optimized the particle density and particle size distribution and then samples were made with aluminium clusters on a glass substrate with silicon nitride or amorphous silicon on top. The entire process takes place in high vacuum, so the aluminium is not oxidized. Some samples were taken out of the vacuum system for 10 minutes in order to oxidize so that the effect of oxidized and metallic particles could be compared.

The samples were characterized using atomic force microscopy and Raman spectroscopy. The a-Si and Si_3N_4 layer thicknesses were determined using DEKTAK. The optical properties of the samples were measured using the Agilent Cary UV-Vis spectrophotometer with integrating sphere. With the integrating sphere, the diffuse reflection caused by scattering could be measured separately.

To support the experiments simulations were carried out using Lumerical FDTD software. Finite differential time domain (FDTD) is a method to solve Maxwell's equations in real time. The resonance wavelength and the scattering and absorption cross-sections were calculated for a range of particle sizes using different silicon or silicon nitride layer thicknesses. These simulations pointed us in the right direction for the experiments and could confirm the shift in the resonance if observed.

Finally, the results of the optical measurements were related to the properties of the sample such as the cluster density and cluster size. The results were compared with the FDTD simulations and the similarities and differences discussed and explained.

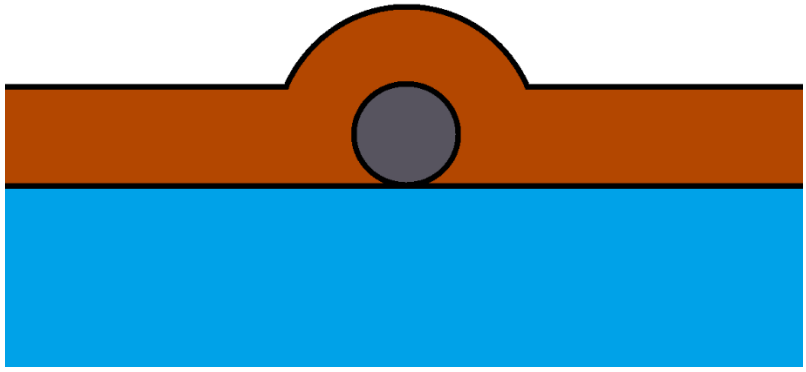

Figure 2. Schematic representation of the aluminium nanoparticle (grey) embedded in amorphous silicon nitride or amorphous silicon (brown) on glass (blue). The silicon and silicon nitride is presumed to grow conformally around the particle.

Theory (2)

Plasmonics of a metal sphere (2.1)

Amorphous silicon solar cells have poor absorption in the red and near infrared due to its high band gap of about 1.7 eV. To increase the efficiency of a-Si:H cells the absorption of light in this part of the spectrum needs to be increased. Light trapping with plasmonic scattering is a technique to increase the optical path length and trap incoming light. In this research we used aluminium nanoparticles in the forward scattering configuration. The resonance frequency of aluminium nanoparticles in the quasistatic limit r<<λ is $\frac{\omega p}{\sqrt{3}}$ at 143 nm in air, which is far in the UV[7]. The resonance frequency can be shifted by embedding the nanoparticles in a dielectric. The resonance is red-shifted as the dielectric constant of the surrounding material is increased. To understand the interaction of the nanoparticles I will give a short theoretical background on the interaction of metal nanoparticles with electromagnetic radiation in the UV-Vis-IR range of the spectrum. The interaction of radiation with spherical particles is fully described by Mie theory. Here I will use the quasistatic limit, which is sufficient since for our particles as r<<λ. In the quasistatic limit the field is assumed to be constant throughout the particle, but the fields are still time dependent. The FDTD simulations incorporate full electrodynamic effects such as retardation, which is ignored in the quasistatic limit.

Drude metal (2.1.1)

A simple approach to describe the effect of radiation on a metal is by using the Drude model. In this approximation the motion of all the electrons is driven by the incident electric field and it is damped by interactions which depend on a constant and the velocity of the electrons. This gives the following equation of motion:

$$m * \frac{d^2 r}{dt^2} + m * \Gamma \frac{dr}{dt} = eE_0 e^{-i\omega t} \tag{2.1}$$

Where m is the electron mass, e the electron charge and Γ the bulk Drude damping constant.

This equation has the following solution:

$$r(t) = \frac{e}{m(\omega^2 + i\Gamma\omega)} E(t) \tag{2.2}$$

So for the polarization P we have:

$$P = -\frac{n*e}{m(\omega^2 + i\Gamma\omega)} E(t) \tag{2.3}$$

Where n is the free electron density.

Using: $\varepsilon = 1 + \frac{P}{\varepsilon_{0E}}$ we obtain the following equation for the dielectric function of a Drude metal.

$$\varepsilon = 1 - \frac{\omega_p^2}{\omega^2 + i\Gamma\omega} \tag{2.4}$$

Where $\omega_p^2 = \frac{ne^2}{\varepsilon_0 m}$

[7] (Blaber, 2007)

If ε_1 is the real part of the dielectric function and ε_2 the imaginary part, we have the following equations:

$$\varepsilon_1 = 1 - \frac{\omega_p^2}{\omega^2+\Gamma^2} \tag{2.5}$$

$$\varepsilon_2 = \frac{\omega_p^2 * \Gamma}{\omega(\omega^2+\Gamma^2)} \tag{2.6}$$

For very low frequencies compared to Γ, ε_2 is much larger than ε_1 and metals are absorbing. The imaginary component of the dielectric function is associated with the real part of the conductivity. For intermediate frequencies, $\Gamma < \omega < \omega_p$, the metal will be reflecting. For high frequencies where $\omega > \omega_p$ the metal can carry waves and the transmission is greater than zero.

When $\Gamma << \omega$, the dielectric functions can be approximated with the following equations:

$$\varepsilon_1 \approx 1 - \frac{\omega_p^2}{\omega^2} \tag{2.7}$$

$$\varepsilon_2 \approx \frac{\omega_p^2 * \Gamma}{\omega^3} \tag{2.8}$$

In real metals the dielectric function is not fully described by this model. There are interband transitions which alter the dielectric function completely and they dominate the optical behaviour of metals such as gold and copper. Aluminium is a relatively simple metal in the sense that its dielectric function is similar to that predicted by the Drude model.

Quasistatic solution (2.1.2)

Now we consider a spherical metal particle surrounded by a dielectric in an electric field. The potential and the electric fields are found by solving the Laplace equation. This yields the following result for the field inside the metal particle:

$$E_i = E_0 * \frac{3\varepsilon_m}{\varepsilon+2\varepsilon_m} \tag{2.9}$$

Where ε_m is the dielectric constant of the material around the particle and ε is the dielectric function of the metal particle. The polarizability of the sphere with radius r is then:

$$\alpha = 4\pi\varepsilon_0 r^3 \frac{\varepsilon-\varepsilon_m}{\varepsilon+2\varepsilon_m} \tag{2.10}$$

This is for a constant electric field, but if $r << \lambda$, the quasistatic approximation for a particle in an electric field can be used even when the electric field is oscillating. The field is then assumed to be constant throughout the particle but the field is still time dependent. This means that the static solution can be used but the dielectric functions ε_m and ε become functions of ω.

Looking at the equation for the polarizability, there is a resonance when $|\varepsilon + 2\varepsilon_m|$ approaches zero. This means that $[\varepsilon_1(\omega) + 2\varepsilon_m]^2 + [\varepsilon_2(\omega)]^2$ should be minimized for a resonance to occur. For that to happen, $\varepsilon_1(\omega)$ needs to be negative and $\varepsilon_2(\omega)$ must be small. This is only the case in metals, which is why metals feature strong plasmonic resonances.

If we assume that $\varepsilon_2(\omega)$ is very small we can use the simplified expression for the dielectric function for ω>>Γ: $\varepsilon_1 \approx 1 - \frac{\omega_p^2}{\omega^2}$ to find the resonance condition. If we take $\varepsilon_m = 1$ then the resonance condition$[\varepsilon_1(\omega) + 2\varepsilon_m] = 0$ gives the following result: $\omega_d = \frac{\omega_p}{\sqrt{3}}$.

Where ω_d is the dipole resonance of the metal nanoparticle.

From the resonance condition: $[\varepsilon_1(\omega) + 2\varepsilon_m]^2 + [\varepsilon_2(\omega)]^2$ it can be seen that if $\varepsilon_m$increases, $\varepsilon_1(\omega)$ must decrease. From the equation: $\varepsilon_1 = 1 - \frac{\omega_p^2}{\omega^2+\Gamma^2}$ it follows that ω must then decrease. As for the magnitude and sharpness of the resonance, ε_2 will increase as ω decreases. This is true for most metals. This gives us an important result: *increasing the dielectric constant of the material around a metal nanoparticle redshifts the resonance while making it broader and weaker. This decrease in sharpness of the resonance is caused by a nonzero* ε_2.

The scattering and absorption cross sections of the metal particle in the quasistatic approximation can be found by considering the Poynting vector of the fields of a dipole illuminated by a plane wave (Maier, 2007).

For the scattering cross section we have the following equation:

$$C_{sca} = \frac{8\pi}{3} k^4 r^6 \left|\frac{\varepsilon-\varepsilon_m}{\varepsilon+2\varepsilon_m}\right|^2 \quad (2.12)$$

Where $k = \frac{2\pi}{\lambda}$. For the absorption cross section we have:

$$C_{abs} = 4\pi k r^3 * Im\left[\frac{\varepsilon-\varepsilon_m}{\varepsilon+2\varepsilon_m}\right] \quad (2.13)$$

These are the cross sections for any spherical particle in the quasistatic approximation, not just for metals. The scattering cross section scales with r^6 and the absorption cross section scales with r^3, which is why the absorption dominates for small particles. For enhancement of optical absorption in a thin film cell large particles which scatter the incoming light are needed. Keep in mind that so far we have only considered the dipole resonance by restricting ourselves to the quasistatic approximation and have neglected higher order modes which are present in larger particles.

Schottky Layer (2.1.3)

When a metal is brought in contact with a semiconductor, the difference in Fermi level causes a transfer of charge until the Fermi levels are equal. For small spherical particles, the effect is different than for bulk metal and dielectric interfaces. The theory for intrinsic amorphous silicon in contact with a metal nanoparticle has been described by (Zhdanov, 2002) and (Verikios, 1996).

This approach models the Schottky layer as a layer of constant thickness around the sphere with uniform charge density. Critical parameters are the width of the depletion layer and the charge that is transferred, as a function of particle radius and the difference in the work function of the metal and the dielectric.

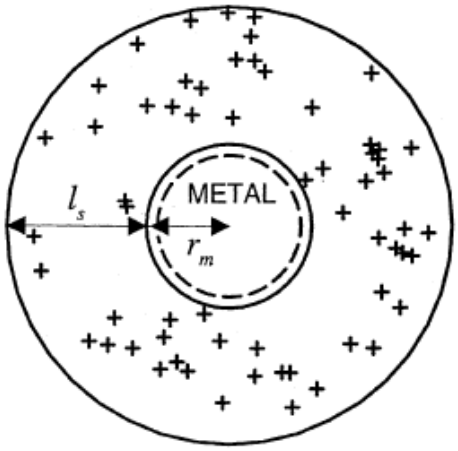

Figure 3: Schematic image of the metal particle and the distribution of charge after charge transfer

For the depletion width W, when W >> r we have:

$$W = L + r = \sqrt[3]{\frac{3\epsilon_s r V_0}{eN_d}} + r \qquad \text{(Zhdanov, 2002) (2.14)}$$

L is the depletion length
ε_s is the permittivity of a-Si
V_o is the barrier height
e is the electron charge
N_d is the number of donors

From here we can calculate the number of electrons transferred:

$$N_e = \frac{4\pi N_d}{3} * (W^3 - r^3) \qquad \text{(Verikios, 1996) (2.15)}$$

The transferred electrons shift the plasmon resonance according to:

$$\omega_p = \sqrt{\frac{N*e^2}{m_0*\varepsilon_0}} = \sqrt{\frac{(N_a+N_c)*e^2}{m_0*\varepsilon_0}} \qquad \text{(Verikios, 1996) (2.16)}$$

where N_a and N_c are the densities of conduction electrons and additional transferred electrons
m_0 is the effective mass of the electrons
ε_0 is the permittivity of vacuum

The peak of the plasmon resonance surrounded by a dielectric is given by the following function:

$$\lambda_{peak} = \frac{2\pi c\sqrt{\varepsilon_m + 2\varepsilon_{si}}}{\omega_p} \qquad \text{(Mulvaney, 2001)(2.17)}$$

where c is the speed of light
ε_m is the high frequency dielectric constant of the metal
ε_{Si} is the dielectric constant of the silicon

This is a somewhat crude approach since this applies to n-doped silicon and for intrinsic materials a value for the number of donors need to be assumed. This makes our approach a rough approximation. This approximation gives us an estimate of the amount of charge transferred and the size of the depletion region.

Size effects (2.1.4)

There are two types of size effects when going beyond the quasistatic limit and the Drude model. Extrinsic size effects because of retardation and intrinsic size effects because of surface scattering, surface damping and other effects where the properties of the electrons in the metal depend on the size of the particle.

For small nanoparticles where r<<λ, the quasistatic approximation is valid. If the radius of the particle increases, the field will not be the same throughout the particle and full Mie theory needs to be used. I will not discuss Mie theory here, but I will give the main effects of an inhomogeneous electric field on the resonance of a metal nanoparticle. This is the extrinsic size effect.

There retardation of the driving field and the retardation of the depolarization field cause a redshift in the resonance. Furthermore, there is radiative damping, the decay of collective oscillations of electrons into photons. Overall, the resonance is red-shifted and broadened. Also, there are higher order resonances than just the dipole resonance from the quasistatic approximation, quadrupoles and possibly even octopoles and so on. In this thesis these effects beyond the quasistatic limit are not solved analytically but they are approximated through FDTD simulations which are suited to the complex geometry of our samples.

There are also intrinsic size effects, where the size of the particle influences its electronic properties. The most important of these is surface damping of the electrons, which has been incorporated in the FDTD simulations through a modified dielectric function for aluminium. The equation of motion we used to calculate the dielectric function uses the damping constant Γ as a material parameter. This damping constant is the bulk damping constant which is related to the mean free path length l and Fermi velocity v_f by the following relation: $\Gamma = v_f/l$. For aluminium this free path length is 16 nm at room temperature (Ashcroft, 1976). For our particles, with typical radii of 5 to 8 nanometer, this means that the bulk mean free path length is larger than the diameter of the particle. Therefore, the mean free path of the electrons needs to be adjusted and a size dependent term is added.

This term, l_r, is found by integrating the scattering over the entire sphere. If the angular dependence of each scattering event is isotropic this leads to $l_r = r$, if the scattered electrons have an isotropic density this leads to: $l_r = \left(\frac{4}{3}\right) r$.

With this term, Γ becomes $\Gamma(\mathrm{r})$, with the following equation:

$$\Gamma(r) = \Gamma_\infty + \Delta\Gamma(\mathrm{r}) \tag{2.18}$$

Where: $\Delta\Gamma(\mathrm{r}) = \mathrm{A} * \frac{v_f}{r}$ and Γ_∞ is the bulk damping constant. The factor A can be equal to 1 or to $\left(\frac{4}{3}\right)$, depending on the choice for either the scattering or the density of scattered electrons to be isotropic. In this research $\left(\frac{4}{3}\right)$ was chosen. The r^{-1} dependence of $\Delta\Gamma(\mathrm{r})$ makes surface scattering the dominant term for small particles.

This damping effect changes the dielectric function according to (Kreibig&Vollmer, 1995):

$$\varepsilon(\omega, r) = \varepsilon_{bulk}(\omega) + \omega_p^2 \left(\frac{1}{\omega^2+\Gamma_\infty^2} - \frac{1}{\omega^2+\Gamma(r)^2}\right) + i\frac{\omega_p^2}{\omega}\left(\frac{\Gamma(r)}{\omega^2+\Gamma(r)^2} - \frac{\Gamma_\infty}{\omega^2+\Gamma_\infty^2}\right) \tag{2.19}$$

Figure 4 shows the dielectric function and the damping adjusted functions for a radius of 8nm.

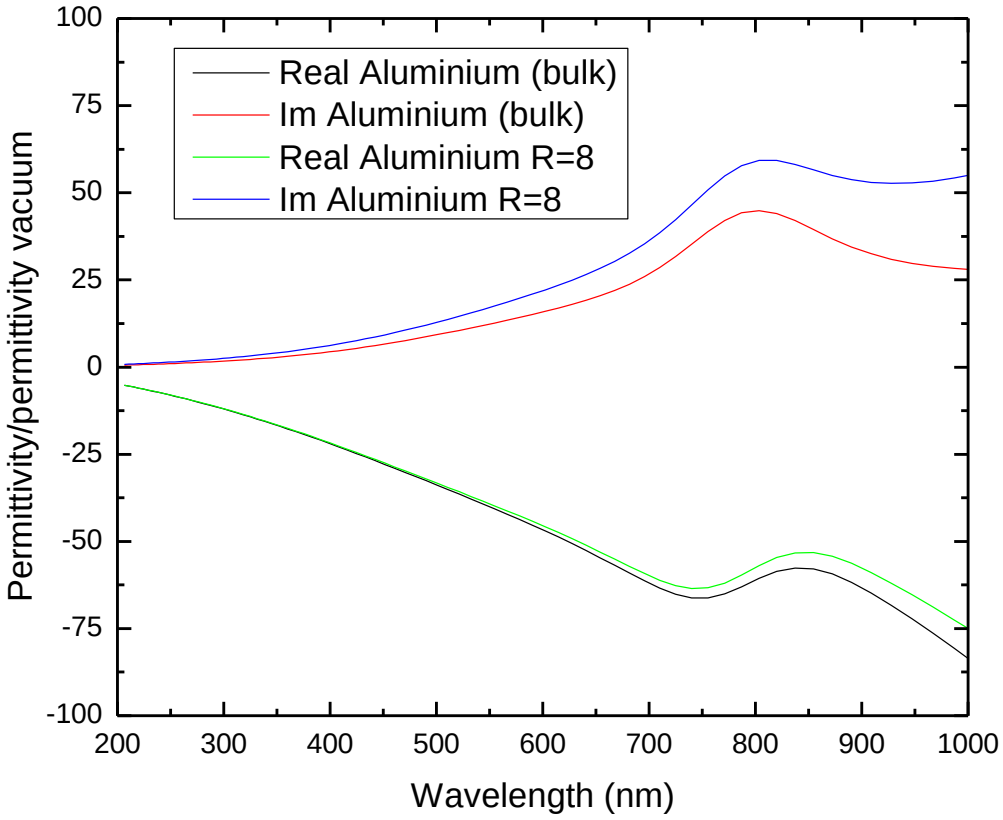

Figure 4. Dielectric function of bulk aluminium compared with the damping adjusted dielectric function for R=8. The biggest difference is in the imaginary component of the dielectric function, which is associated with the real conductivity

There are other intrinsic size effects such as chemical interface damping described very well by Kreibig and Vollmer in the book 'Optical properties of metal clusters'. Depending on the theoretic model used and the materials involved these can cause a blue- or a redshift compared to standard Mie theory.

Ensembles of particles (2.1.5)

Inter-particle interactions cause a blue-shift or a redshift depending on their relative orientation. For the samples in this thesis the particles are not positioned in an array but are spread randomly over the surface. There is also a range of particle sizes present in our samples, which will broaden the sum of the resonances of the particles. Detailed studies on arrays of plasmonic particles have been done, in the case of regular arrays.[8] These studies found that long range interactions, which are associated with electrodynamic effects, cause a blue-shift of the resonance. When the inter-particle distance is smaller than the plasmon wavelength electrostatic interaction dominates and this causes a redshift and a broadening of the resonance. In a regular array, the short range interaction also depends on the polarization of the light. If the polarization is in the direction of the array, the resonance is red-shifted as the dipoles counteract each other. For transverse polarization, the resonance is blue-shifted. This is illustrated in the following image, figure 5.

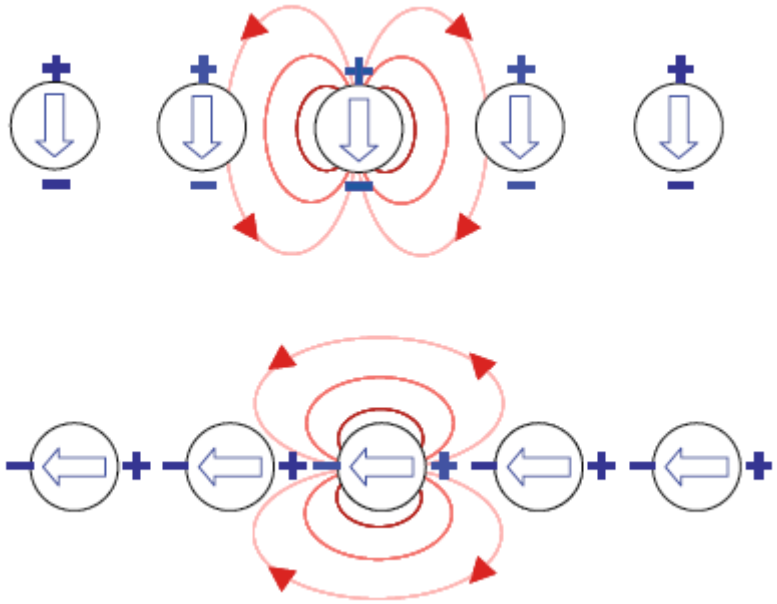

Figure 5. Schematic of transverse (top) and longitudinal polarized light on a particle array. Image taken from (Maier, 2007).

These short range interactions scale with the inter-particle distance d^{-3}. This means that those interactions fall off rapidly with increasing distance. Maier states that 150 nm is a typical distance for which the short range interaction is almost negligible. Zhao et al take the plasmon wavelength as a cutoff criterion for the inter-particle distance for which electrostatic interactions are negligible. In our samples, the typical distance between particles is in the order of 200-300 nm, but some pairs are closer. This means that there may still be a small contribution of a near field interaction on these particles. As we work with unpolarized light, this could lead to a small broadening of the resonance.

[8] (Zhao, 2003), (Turan, 2010), (de Waele, 2007)

Electrodynamic interactions between plasmonic particles dominate for larger inter-particle distances, as these scale with d^{-1}, described by Lamprecht et al. on a regular array of gold nanoparticles. They found[9] that there was a blue- or a red-shift depending on the inter-particle distance and that there was a broadening of the resonance, for particle distances in the range of 400-900 nm. However, they also found that no significant shift or broadening for random arrays are found for random ensembles of nanoparticles for an inter-particle range between 400 and 1000 nm. Our typical inter-particle distance is smaller so there may still be some broadening of the plasmon resonance due to electrodynamic effects.

Generally speaking, all effects we discussed that go beyond the quasistatic approximation cause a broadening of the plasmon resonance. Retardation causes a red-shift, embedding the particles in a dielectric causes a red-shift. Surface damping causes a slight blue-shift but mostly broadens the resonance and the Schottky layer and the charge transfer causes a slight blue-shift of the plasmon resonance was well, but the changed optical properties of the surrounding dielectric also need to be considered.

[9] (Lamprecht, 2000)

Methods (3)

Cluster and sputter source depositions (3.1)

The clusters were deposited on glass samples with a thickness of 2-3 mm of around 1 cm^2. The glass has a typical roughness of the order of 1 nm. The glass samples were cleaned by sonication in isopropanol for 3 minutes before being inserted in the vacuum system. The vacuum system features a load lock for fast sample loading and unloading, a central chamber for the cluster source depositions, a cluster source and a sputter chamber. A picture of the vacuum system is presented below in figure 6.

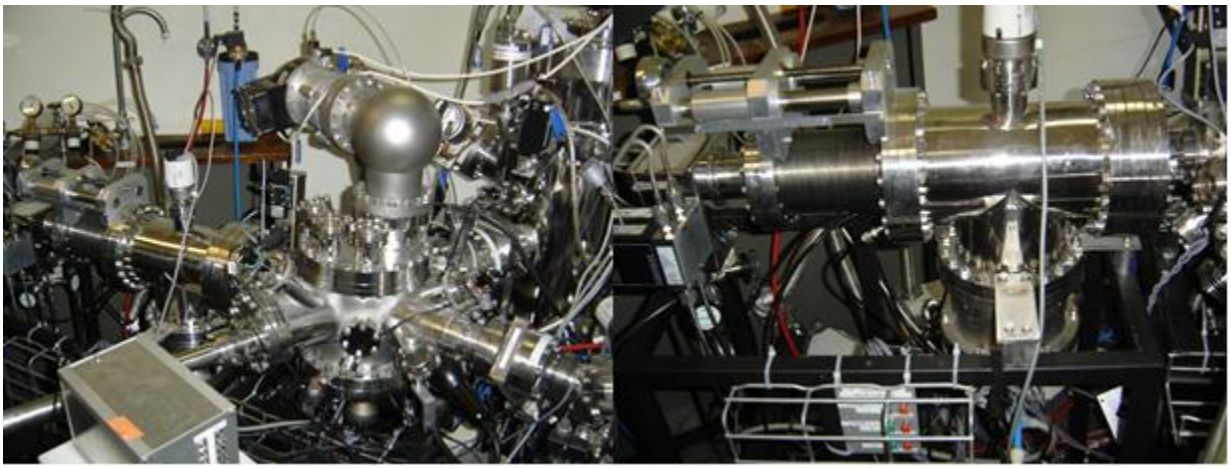

Figure 6. Left image: 'Zeester' vacuum system. The samples are brought into the central chamber. On the left is the cluster source. Right image: cluster source. The agglomeration length can be controlled by adjusting the column on the left.

The Oxford Applied Research NF-200B cluster source was used with an aluminium target to deposit the aluminium nanoparticles on glass. In the cluster source aluminium is sputtered through magnetron sputtering with an Argon or Helium plasma. Both DC and RF sources can be used to power the magnetron, in this research the DC source was used because this yields more particles with the conducting aluminium target.

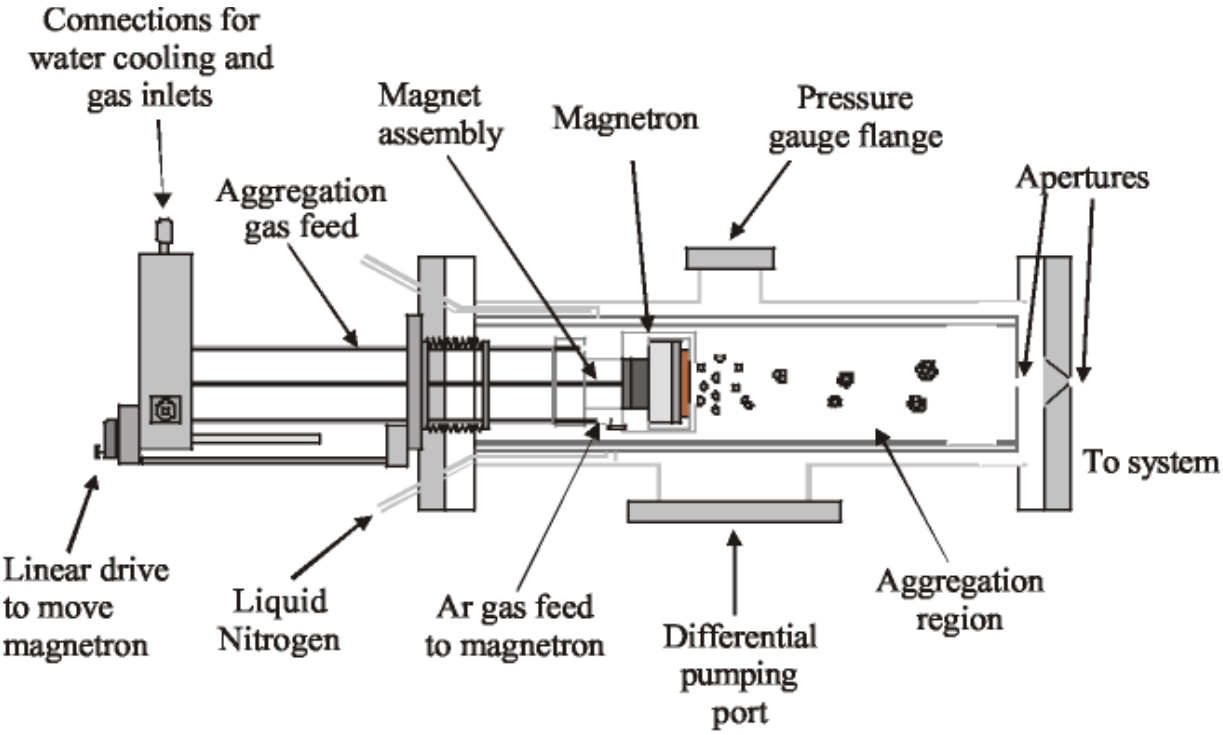

Figure 7a. Overview of the cluster source. Image taken from Ref (R.Smith).

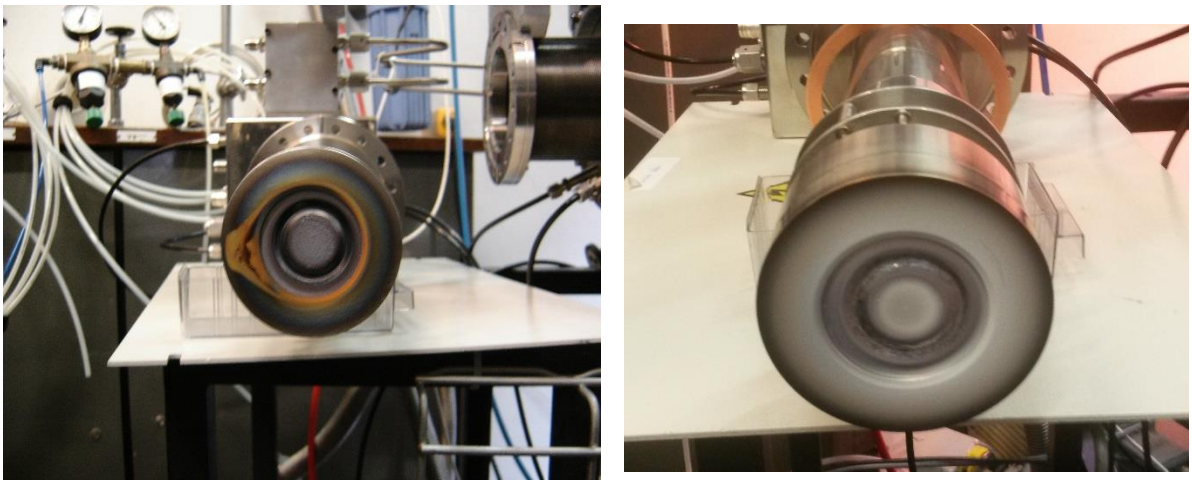

Figure 7b. Pictures of the magnetron head. The characteristic annular sputtering pattern is clearly visible on the target. The argon is fed through a mm-sized annular opening between the disk-shaped target and the magnetron. A DC voltage is applied between the magnetron and the target and there is a strong fixed magnet behind the target. Ionized argon atoms strike the target surface and release material from the target. The released material diffuses through the aggregation region and condenses into clusters and moves through the aperture or settles inside the agglomeration region. The brown dust in the left image consists of silicon particles from previous work. The image on the right was taken after many aluminium depositions. The white dust consists of oxidized aluminium.

The sputtered atoms can agglomerate in the cluster source to form clusters of particles. The formation of clusters occurs when atoms can lose their energy to the Argon or Helium gas stream in the cluster source. The stream of gas carries the particles from the cluster source to the central chamber where it hits the sample and particles are deposited. The gas stream from the cluster source to the central chamber is driven by the pressure difference between these chambers.

The cluster size and density can be manipulated by changing the gas flows, the agglomeration length in the cluster source the magnetron current and the deposition time. Generally speaking, increasing the agglomeration length increases the particle size; increasing the Argon gas flow increases particle size and increases the sputtering rate. There is an optimum current, after which increasing the current leads to a decrease in sputtering rate. Increasing the deposition time increases the particle density, although at high particle densities the particles may agglomerate on the sample if they are mobile. An overview is given below in table 1.

	Cluster size	Deposition rate
Agglomeration length	Increase	Increase
Gas flow	Increase	Increase
Helium added	Decrease	n/a
Power	Optimum	Optimum

Table 1. Relation between the parameters of the cluster source and the resulting deposition.[10]

The cluster source is a complex system and a combination of changing parameters simultaneously can yield different results than one would expect based on changing parameters one at a time. Depositions done with the exact same parameters can yield different results if they are done a few weeks apart. Generally speaking, the shorter the delay between depositions the higher the chance that the results are similar.

The substrate also influences the cluster size and the density. The clusters need to stick to the surface, but they can also migrate and even merge. The degree to which this occurs depends on the interaction between the surface and the clusters. Many of the clusters are charged and this can also influence the deposition rate, especially for conducting surfaces.

After cluster deposition the sample can be moved directly to the sputter chamber for deposition of a layer of silicon or silicon nitride without leaving the vacuum system. This prevents the aluminium clusters from oxidizing. The layers of silicon and silicon nitride are produced via magnetron sputtering in the large vacuum chamber using an argon gas feed. The large vacuum chamber produces amorphous layers of silicon nitride or silicon. The relation between the layer thickness and the deposition time is constant over many depositions.

[10] Taken from NC-200 U test data by OAR

Topography: DEKTAK (3.2)

Characterization of the topography of the samples was performed with AFM and DEKTAK. DEKTAK was used to measure the thicknesses of the silicon and silicon nitride layer, AFM was used to determine the cluster size and cluster density.

The Bruker DEKTAK XT profilometer was used. This machine operates by scanning the sample surface with a diamond tipped stylus. This stylus is moved over the surface continuously, meaning there is always contact between the tip and the sample. The force between the tip and the surface can be controlled by the user. This makes DEKTAK suited for measuring very hard as well as very soft surfaces.

The stylus can move over large distances (up to 1cm). This makes DEKTAK a good technique for measuring the thickness of a deposited layer on a solid surface, where there is a transition between one height and another over a large distance. The vertical resolution is op to 1nm, depending on the sample. However, it is very difficult to determine the thickness of an ultrathin layer (<20nm) unless the substrate is extremely flat. Otherwise, the roughness of the substrate will dominate and it becomes impossible to determine the step location or step height.

The output data is a dataset of the height versus the horizontal position. This data can be processed and analyzed to determine parameters such as the surface roughness or a step height. To determine the step height we needed to identify the glass and the silicon nitride or the silicon and flatten the curve accordingly. An example is given in the image below. The measurement was carried out at least 6 times on each sample and the error was determined by the standard deviation of the step height.

Topography: Atomic force microscopy (3.3)

Atomic force microscopy (AFM) is a technique to measure the topography of a sample in high detail. A fine needle called a tip scans the surface of the sample. In this research the AFM was used in tapping mode; which means that the tip is not constantly in contact with the sample. The operating principle is as follows.

The tip is positioned at the end of a cantilever which is oscillating near its resonance frequency (200-300 kHz). When the tip approaches the surface, interaction between the tip and the surface will dampen the oscillation. As the tip moves horizontally over the sample surface, the amplitude of the oscillation is held constant by the feedback loop and this results in a vertical profile. The amplitude and frequency are measured by reflecting a laser off the surface of the cantilever. The reflected beam hits a detector. The horizontal position is controlled by piezoelectric elements and the tip scans the surface line by line. A schematic is given in figure 8. [11]

[11] Taken from Veeco SPM manual, 2005

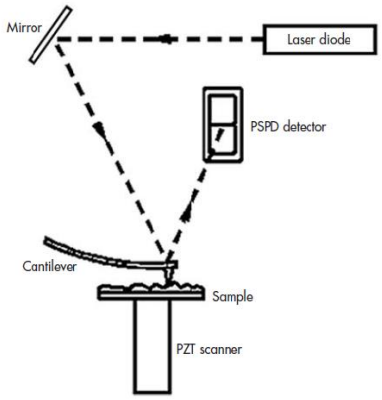

Figure 8. Schematic representation of AFM. The reflected laser light hits a detector. A feedback loop keeps the amplitude constant. This feedback loop gives the vertical profile.

In contrast with DEKTAK, AFM gives a map of the sample height versus horizontal position in a plane, rather than a single line. This means that only a small part of the sample can be measured; typical measurements in this research are 10 by 10 µm. The vertical resolution is very high (<1nm) as the height of each position is sampled numerous because of the high oscillation frequency. The horizontal resolution is much lower since it is controlled by piezoelectric elements and it is not measured directly. Also, the tip will deteriorate over time and can become less sharp, which reduces horizontal resolution. The feature size must therefore be deduced from the vertical profile and not the horizontal image.

Raman spectroscopy (3.4)

Raman spectroscopy is a technique which relies on inelastic scattering of monochromatic light from the sample. Laser light hits the sample and a small fraction of it is scattered inelastically as the light with an atom or a molecule. The atom or molecule is brought into a higher vibrational energy state and this decreases the energy of the scattered photon. The vibrational states depend on the bond between atoms, this makes Raman spectroscopy a powerful tool to analyze the chemical composition of a material.

In our research the Renishaw inVia Raman spectroscope was used. We used the 514 nm 50mW Argon laser to illuminate the sample. The glass and the aluminium target were also measured as a reference.

TEM (3.5)

Transmission electron microscopy (TEM) was performed on particles deposited directly on the holey carbon membrane and on particles embedded in amorphous silicon. Two samples with aluminium nanoparticles deposited directly on the membrane were used and two samples were prepared by scraping flakes of silicon off a glass sample. The flakes were then put on the TEM membrane using isopropanol. It was not possible to scrape flakes off of the silicon nitride samples due to hardness and strong adhesion.

A holey carbon membrane on a copper grid by Ager scientific was used to support the particles. The TEM used was the Tecnai 12 120 kV electron microscope, with a BIOTWIN objective lens with a 0.49 nm point resolution. Images were captured with a CCD and processed using iTEM software. The bright field mode was used.

FDTD (3.6)

In order to simulate the system of an aluminium particle embedded in a thin layer of silicon nitride or amorphous silicon Lumerical's FDTD software was used. FDTD, is a method to solve Maxwell's equations time dependently. Maxwell's equations are discretized by dividing the simulated volume into a large number of volume elements and putting the components of the E-field along the edges of these cubes. The H-field components are normal to the faces of the cube. In the first time step the E-field components are updated and then the H-field components, then the E-field components are updated again and so on. The full dielectric function of the material in each cube is needed to perform this calculation.

The strength of the FDTD method is that it is applicable in almost any situation, as long as the dielectric functions of the materials are known. It is a memory and memory bandwidth intensive method with a low number of instructions per unit of data.

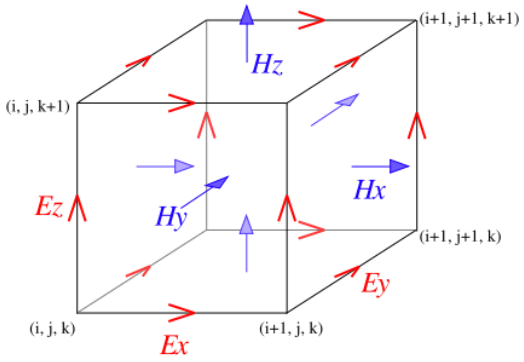

Figure 9. Example of a Yie cell with field components.[12]

It was necessary to perform careful convergence testing. The convergence was tested for the PML layers, the mesh size and the simulation domain size. A small simulated area, smaller than the longest wavelength that is simulated, may distort the results. Around the metal nanoparticle an even finer mesh was used as the regular conformal meshing technique is not reliable around metal-dielectric interfaces. Lumerical FDTD has a solution for this which gives a finer mesh around the metal nanoparticle. Even so, we chose to override the mesh around the nanoparticle. The results for convergence for the mesh around a particle with a radius of 8 nm are shown below in figure 10. A total field-scattered field source was used to determine the scattering cross sections and because a plane wave is not recommended for non-periodic structures, due to edge effects. The injected wave has a Gaussian intensity-energy profile, with wavelengths between 150 or 200 nm and 1000 nm. The 'conformal 0' meshing technique was used on all areas except for the mesh directly around the particle. The pulse width is determined by the user-specified wavelength range, the 'optimize for short pulse' mode was used. Pulse lengths are in the order of 2-8 femtoseconds.

[12] Uploaded under creative commons license to wikimedia by S. G. Johnson, MIT

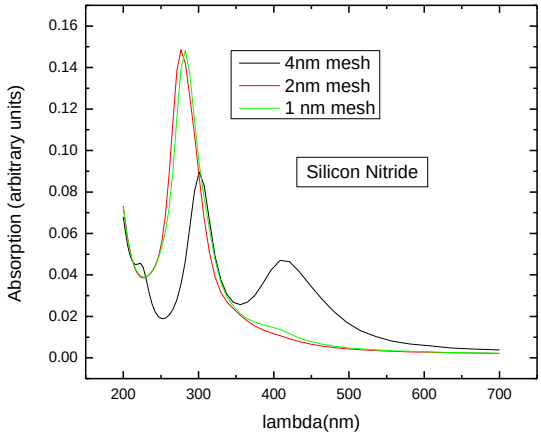

Figure 10. Absorption versus mesh size for an 8 nm particle. The 4nm mesh size gives a false resonance at 430 nm

At a mesh size of 4 nm the particle shows a second resonance at a wavelength of 430. When the mesh size around the particle is reduced to 2nm this peak disappears. The difference between the 1 and 2 nm mesh is marginal. For our simulations we used a 1 or a 1.5 nm mesh. Reducing the mesh size by a factor 2 can increase the simulation time by a factor of 2^4 (16), because the number of elements scales inversely with the volume of the cell and the time step also scales with the size of the cell. It is therefore necessary to find a good tradeoff between accuracy and simulation time.

An example of our setup is given in figures 11, 12 and 13. The materials and the mesh are visible. The orange box denotes the edge of the simulation region. The yellow boxes are monitors which extract data such as the fields or the absorbed power or the scattered fields. The green and blue areas denote the boundary conditions; antisymmetric and symmetric respectively. This way only a quarter of the simulation area is actually solved saving memory and computation time. A pulse of light is injected into the system from the bottom. This source is a total field scattered field source which only lets scattered light through its boundaries. This way a field monitor around the source can be used to calculate the scattering cross section of the particle. The boundary conditions are perfectly matched layers (PML) which absorb all the incoming radiation and the aforementioned periodic boundary conditions.

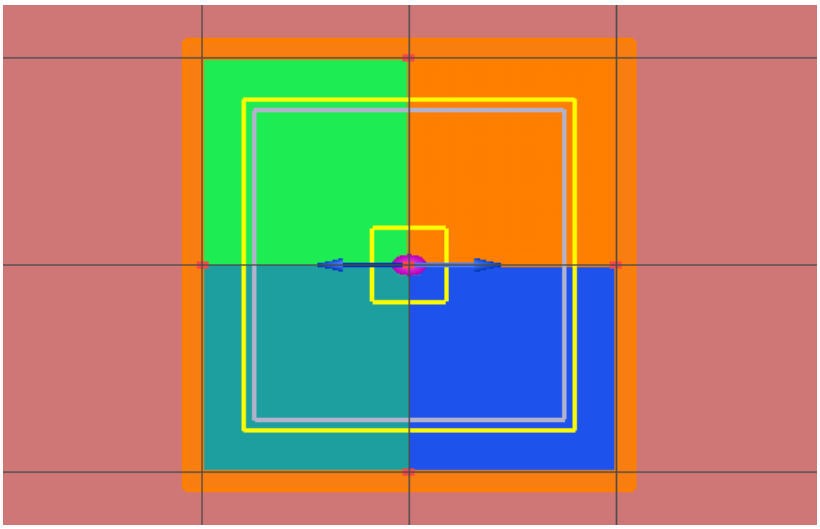

Figure 11. Top (XY) view of the simulated area. The orange box is the simulated area of 2x2 micrometer. They grey box is a TFSF source. The blue arrows illustrate the polarization of the injected wave. The blue and green regions denote anti-symmetric and symmetric boundary conditions, respectively. Because of the symmetry of the sphere only the top right corner is simulated which allows a finer mesh to improve accuracy.

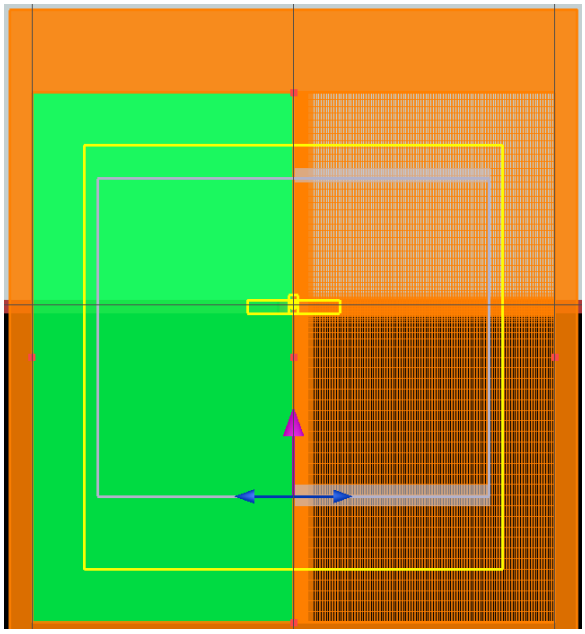

Figure 12. Side (XZ) view of the simulation area. The grey box is the TFSF area of 1.5 by 1.5 micron, the purple arrow is the direction in which the field is injected. The orange mesh is much finer near the nanoparticle and perpendicularly along its axes. The yellow box around the TFSF area is used to measure the scattering cross section. The yellow boxes in the center are used to measure the absorption cross section of the particle and the absorption in the region around the particle.

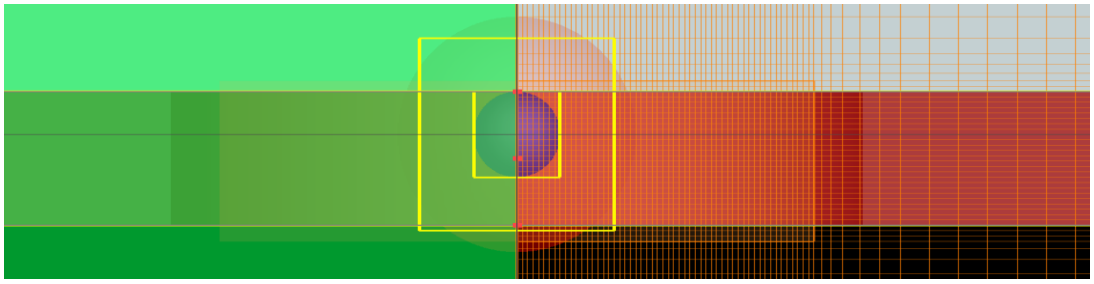

Figure 13. Close-up (XZ) of the area around the particle. The dark red area is the b-doped amorphous silicon, light red normal amorphous silicon. The layer is 25 nm thick and is assumed to grow conformally around the particle. The grey are is the glass, dark blue the particle. The yellow box directly around the particle is to monitor the absorption cross section, the bigger box is to measure the absorption profile directly around the particle.

Results (4)

The composition and topography of the samples were characterized with AFM, Raman Spectroscopy, Transmission Electron Microscopy and DEKTAK. The optical properties were measured using UV-Vis spectroscopy and FDTD simulations were used to predict the effect of the nanoparticles on the optical properties. First the topography of the samples will be discussed. Then the results of the optical measurements will be presented and they will be compared with the FDTD simulations.

Sample topography and composition (4.1)

Overview (4.1.1)

An overview of topography of the final samples that were measured optically is given in table 2.

	Sample	Layer thickness (nm)	Particle density	Average particle size (nm)
Si_3N_4	SS99	23(6)	n/a	n/a
	CS566	23(6)	13(3)	6
	CS585	23(6)	10(2)	12
	CS588	23(6)	17(4)	12
	CS595	23(6)	6(2)	10
	CS596(ox)	23(6)	12(3)	10
	CS599	23(6)	4(1)	15
	CS600(ox)	23(6)	4(1)	15
a-Si	SS127	12(2)	n/a	n/a
	SS126	25(4)	n/a	n/a
	SS131	50(8)	n/a	n/a
	CS608	12(2)	4(2)	8
	CS609	12(2)	8(3)	8
	CS616(ox)	12(2)	7(3)	8
	CS533(ox)*	12(2)	60(10)	20
	CS610	25(4)	4(2)	8
	CS611	25(4)	8(3)	8
	CS615	25(4)	3(1)	6
	CS618	25(4)	6(2)	6
	CS617(ox)	25(4)	8(3)	8
	CS612	50(8)	4(2)	8
	CS613	50(8)	8(3)	8
	CS621(ox)	50(8)	8(3)	8

Table 2. Overview of the samples that were used for optical measurements. CS533 was an anomaly, with 15 SCCM Argon and 5 SCCM Helium gas flow. We were unable to reproduce these results and obtain such high particle densities and large particle sizes again.

Overall, our results confirm the relation between the main parameters of the cluster source and the particle size and density. Increased currents and high gas flows resulted in higher particle densities. A full overview of all samples, is given in Appendix A.

AFM (4.1.2)

The aim during deposition was to produce samples with a particle density as high as possible and a cluster size as large as possible. Three layer thicknesses were used: 12(+-3) nm, 25(+-5) nm and 50(+-6) nm. Note that the error in the thickness is the DEKTAK measurement error; the thickness of the layer is presumed to be nearly constant for different depositions.

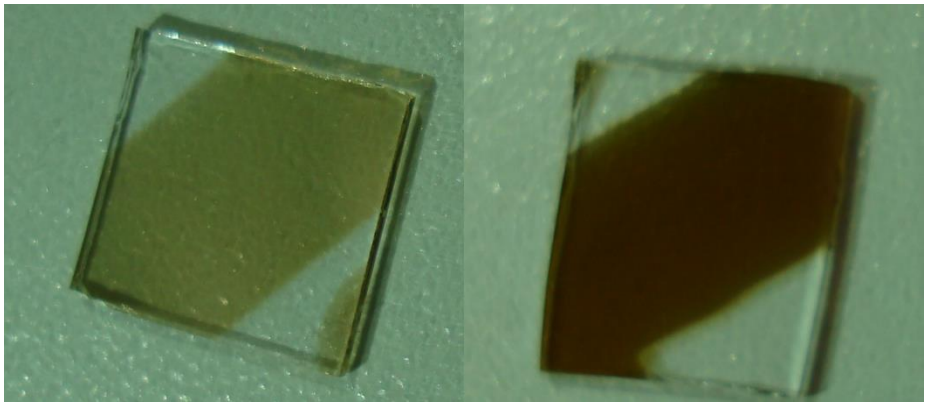

Figure 14. 50 nm layer of silicon nitride (left) and amorphous silicon (right), both with aluminium clusters (CS601&CS621)

Typical densities of particles of a significant size (> 6nm in diameter) were between 5 and 18 particles per square micron. A typical size distribution is shown in the following graph, figure 15. For an overview of the particle size distributions and densities I refer to Appendix A.

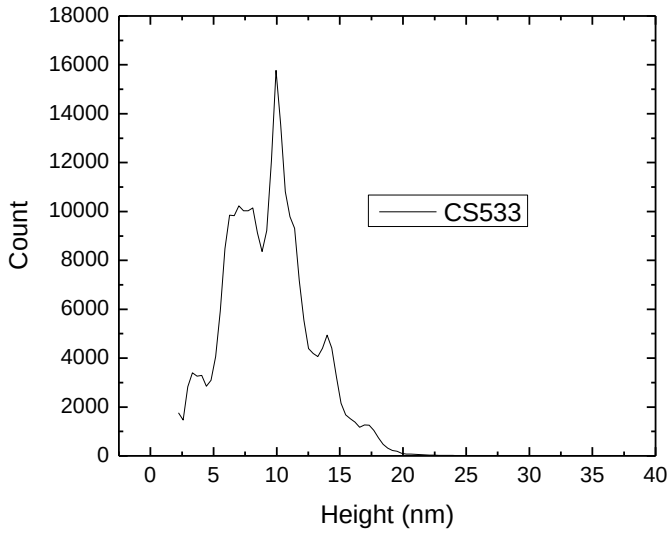

Figure 15. Distribution of feature size obtained with WSXM for CS533. Multiple peaks are seen and the average height is just under 10 nm.

AFM images of the particles as deposited on glass are shown below in figure 16.

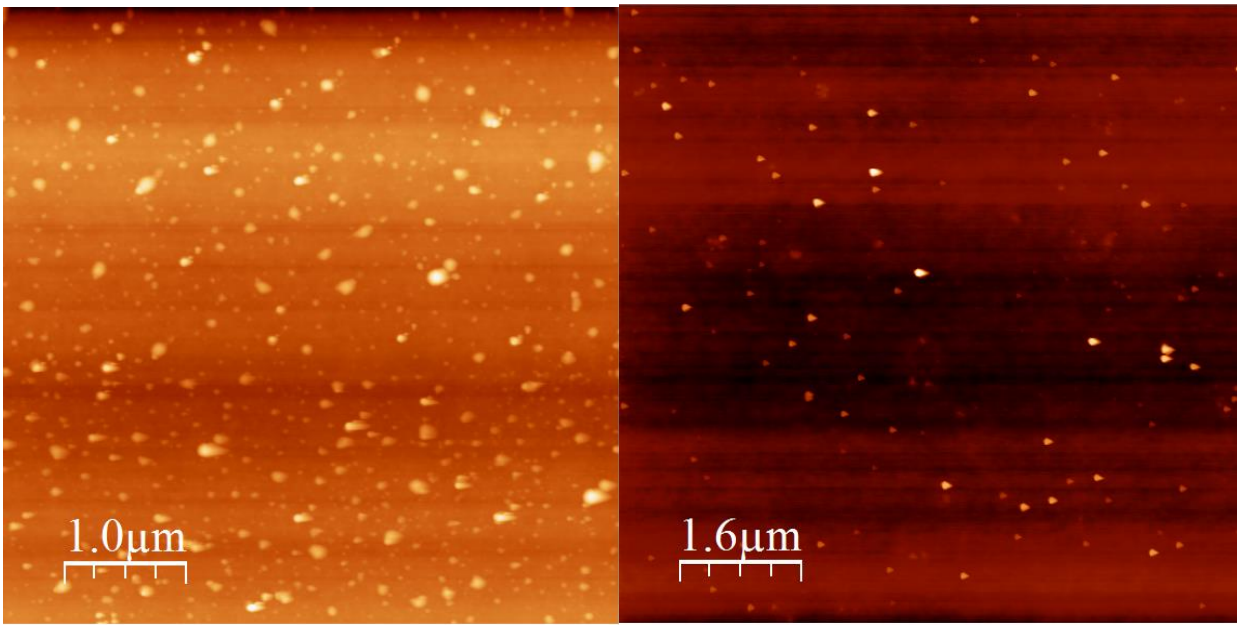

Figure 16. Left: 5x5 µ AFM image of CS586, reference for several Si_3N_4 depositions. Right: 8x8 µ image of CS600, another reference for Si_3N_4 depositions. A 25 nm layer of Si_3N_4 was later deposited on CS600.

Most of the experimental range of the nanocluster source in our setup has been experimentally verified. For more details regarding the nanocluster production see Appendix A. It was found that the optimal settings featured high currents of 0.2-0.25 A, a high Argon gas flow of 20 SCCM and a medium aggregation length of 40 mm.

It should be noted that the nanocluster source does not consistently give the same output. The same settings can be used on two different samples yielding different results, even when the samples are made in one session. There is also a gradual change, where yields decrease over time due to consumption of the aluminium target. Therefore, the particle density is uncertain. To determine the particle density we used the AFM measurements of the silicon nitride and a-Si samples and the reference samples. We also used TEM and Raman spectroscopy to determine the particle density but with limited results.

When covered with silicon nitride, the particles are still visible with AFM when the layer is 12 or 25 nanometers thick. The particles are very difficult to distinguish when covered by the thick 40-50 nanometer layer. Therefore, to determine the particle density is highly uncertain when the layers are thick. The following pictures in figure 17 are AFM images of aluminium clusters with a silicon nitride layer.

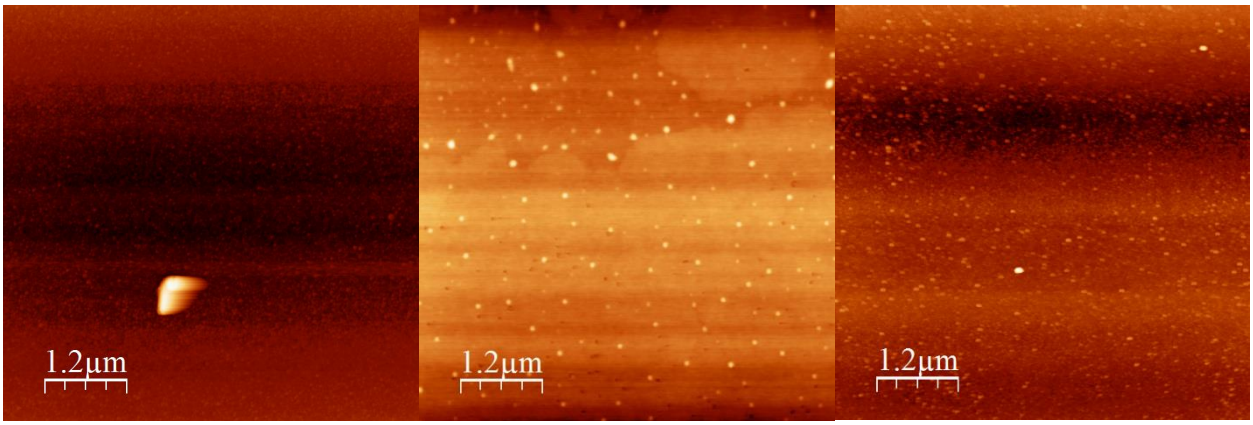

Figure 17. Left: SS99, Si_3N_4 layer with 2-3nm roughness. Center: CS552, +-10 nm aluminium nanoparticles. Right: CS566: aluminium nanoparticles with 25 nm Si_3N_4 layer on top of the particles. The 8-10 nm features have aluminium particles underneath.

With silicon nitride we are able to distinguish potential active aluminium nanoparticles with a radius of at least 4 nm underneath the deposited layer. This is because the roughness of our silicon nitride is in the order of 2 to 3 nm. This makes it possible to determine the particle density from the AFM images.

Another example of a sample and a reference is presented below in figure 18.

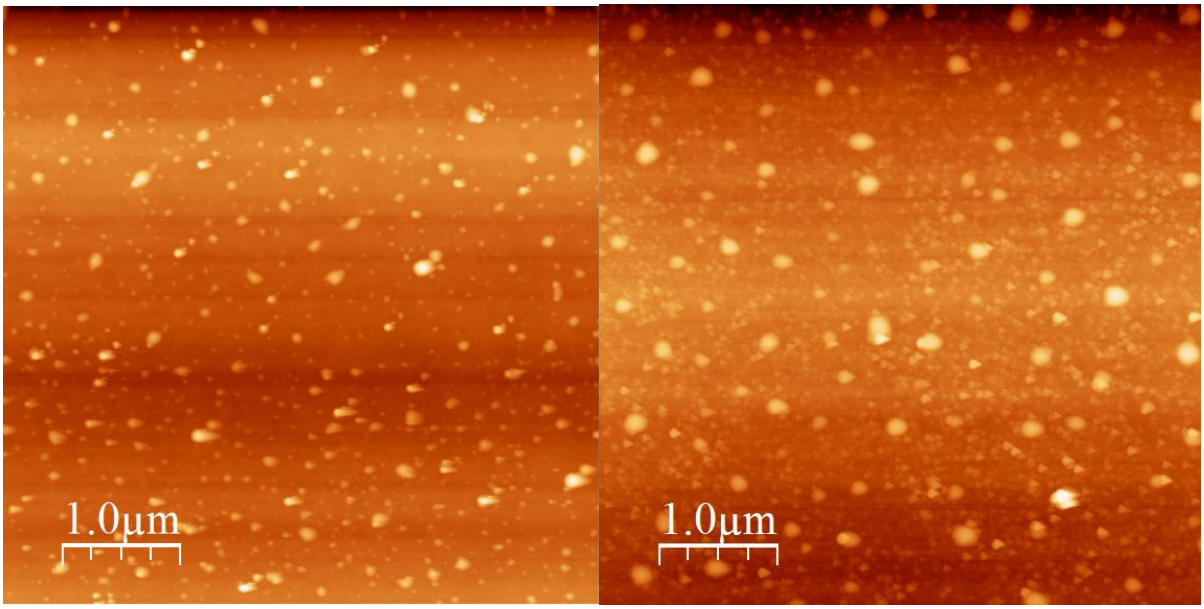

Figure 18. Left: CS586, sample with 5-15 nm nanometer aluminium particles; a reference for many Si_3N_4 depositions. Right: CS585, sample with same cluster deposition parameters as CS586, with a 25 nm Si_3N_4 layer. Features are 5-10 nm in size, which indicates that the Si_3N_4 smoothens some of the roughness underneath. Images are 6x6 µm.

The amorphous silicon was rough and had features of 5-10 nm on top of the layer. This made it very difficult to determine the particle density of a sample with aluminium nanoparticles covered by an amorphous silicon layer based on the AFM images. Particle density was determined from the AFM images of the reference samples without a silicon layer. The particle density was significantly lower compared with the Si_3N_4 depositions which were carried out a few weeks earlier. This could be due to wear of the aluminium target.

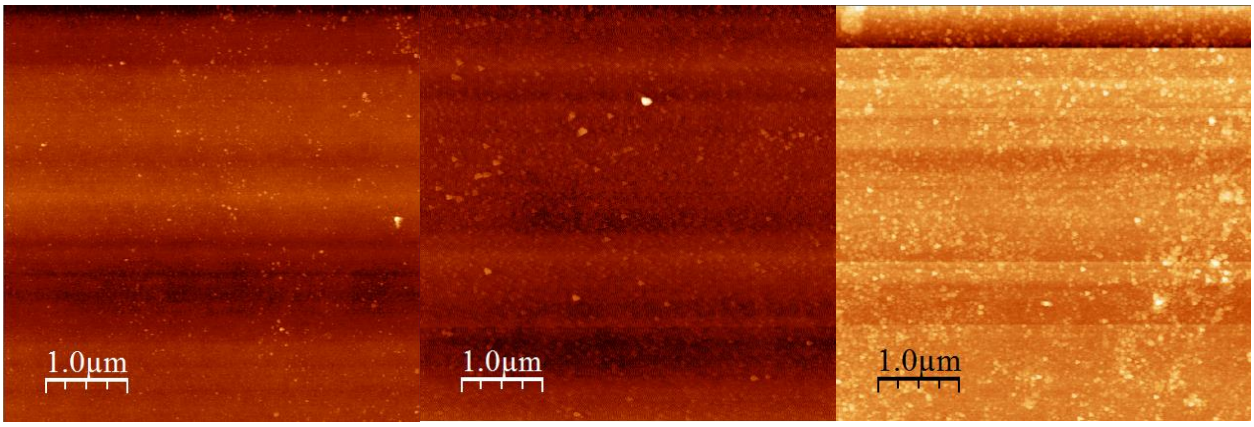

Figure 19. a-Si depositions of 12, 25 and 50 nm layers (left to right). The surface has features of 4-8 nm in size, the density of these features increases with layer thickness. AFM images are 5x5 µm.

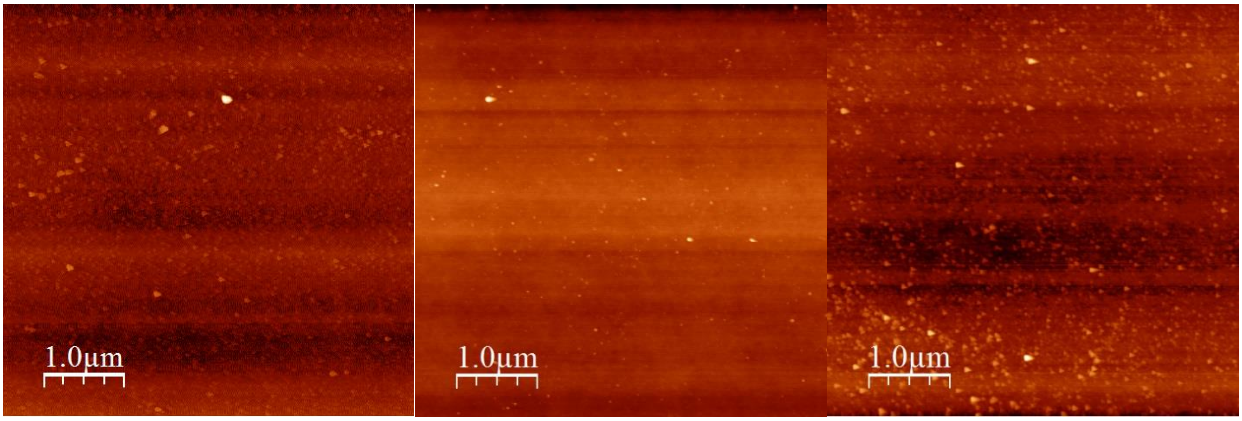

Figure 20. Left: SS126, 25 nm a-Si layer. Center: CS 620, reference aluminium cluster deposition. Features are 3-10 nm in size. Right: CS 615; 5-10 nm aluminium clusters with a 25 nm a-Si layer. There are more features than in the previous two samples combined. Features are 3-12 nm. It is very difficult to distinguish roughness caused by aluminium nanoparticles from the natural roughness of these a-Si layers.

The increased roughness of the amorphous silicon samples compared with the silicon nitride samples could be related to its higher growth rate. In any case, it makes it extremely hard to distinguish the metal particles. This gives us a high uncertainty in the particle density and size distribution.

In order to distinguish morphological effects from plasmonic effects or other effects of metallic aluminium on the optical properties of the samples, some samples were made with oxidized aluminium nanoparticles with Si_3N_4 or a-Si layers. The clusters were oxidized by taking them out of the vacuum system for 10 minutes. Examples of these are displayed in the image below, figure 21.

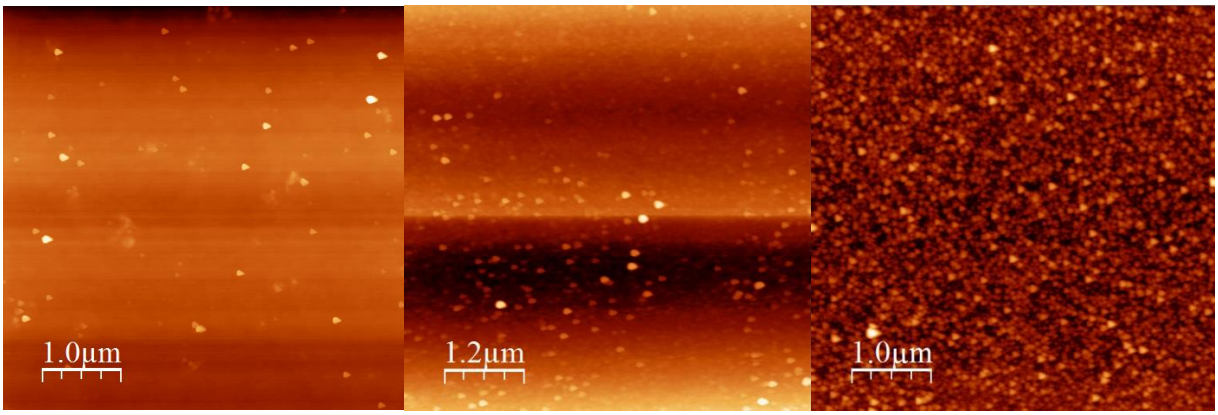

Figure 21. Image 6. Left: CS600; 5x5µm AFM image of aluminium nanoparticles. Center: CS600 with a 25 nm silicon nitride layer on top, 6x6 µm. Right: CS533, a sample with oxidized aluminium nanoparticles with a 10 nm a-Si layer. This sample has a very high particle density and large 15-30 nm particles. Unfortunately we were unable to reproduce these kinds of particle densities.

We also deposited particles on a layer of Si_3N_4/a-Si in order to cover these with a Si_3N_4/a-Si layer. This is done because the particles are then surrounded by a single material instead of both glass and Si_3N_4 or a-Si. This would make the dielectric environment well defined. However, the particle density depends strongly on the substrate and the particle density when deposited on Si_3N_4 and a-Si was very low compared with the regular deposition on glass. This is caused by the nature of the surface interaction between Si_3N_4/a-Si and the aluminium nanoparticles. This could also be caused by some surface charge on the Si_3N_4/a-Si layers after deposition.

TEM (4.1.3)

We were able to scrape some material from two samples with a-Si. The flakes were put on a carbon membrane TEM-grid using isopropanol. One of these is CS533, an AFM image of this sample can be found in *Image 6*. The other is a 12 nm thick a-Si layer. We were unable to scrape material off the other a-Si samples, likely because the silicon atoms are bonded to the glass in those samples. Silicon nitride is harder than glass, so it is impossible to scrape material off the surface without damaging the glass.

The amorphous silicon flakes can be seen clearly in the left image in figure 22. The right image is a flake from CS533, a sample with a high particle density and a 12 nm a-Si layer. The dark areas on the left are stacks of the amorphous silicon with embedded particles. On the bottom right of the image, a single sheet can be seen with a number of particles inside. The particles are dark grey. They have sharp angles, which suggests a crystalline structure. Their size is in the order of 20 nm, similar to what we expected from AFM measurements.

The second image features aluminium particles deposited directly on the TEM grid. The particles have coalesced and oxidized. Many particles have a dark core and a lighter outer layer, which indicates that the outer parts have oxidized. The particles are larger than typical particles for our samples, with a size of 20 to 50 nm.

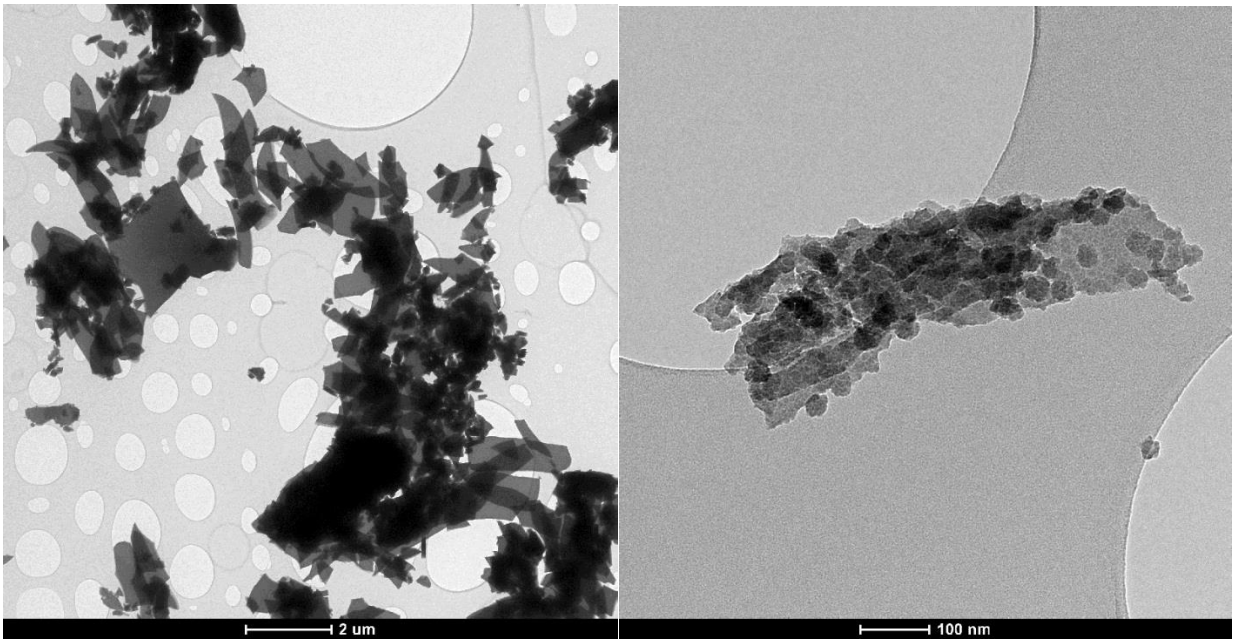

Figure 22. Left: SS127, flakes of 120 nm thick amorphous silicon. Right: CS533, 12 nm thick a-Si layer with oxidized aluminium particles embedded. The image confirms the estimated density of about 50 to 70 per square micron. Cluster size is around 20 nm.

We also deposited aluminium particles directly on the TEM grids. Results are shown in figure 23.

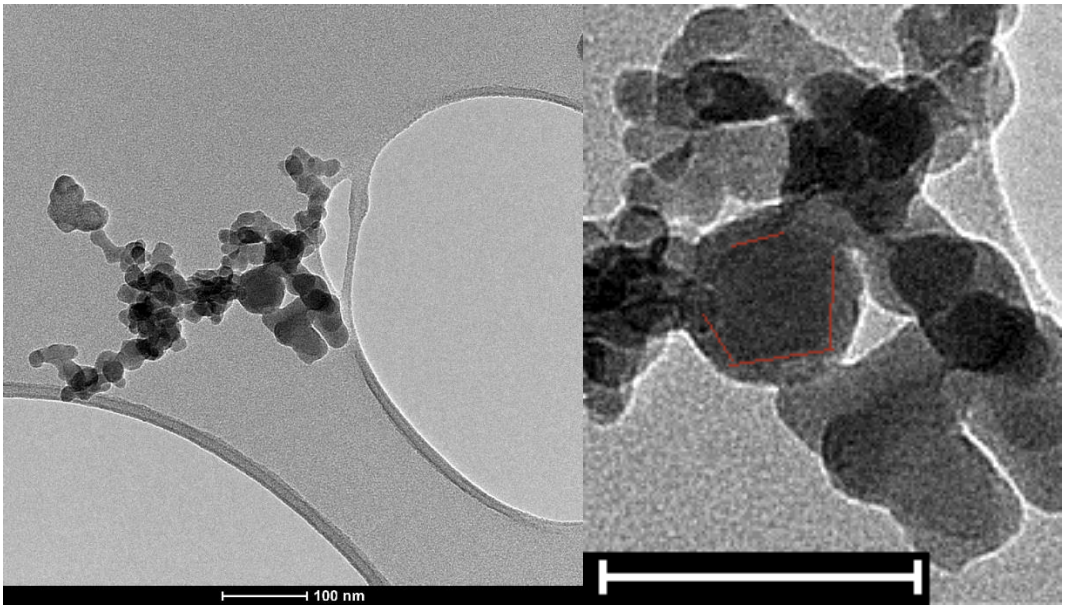

Figure 23. Aluminium nanoparticles on carbon TEM grid. Particle size is between 10 and 50 nm. Particles have oxidized, agglomerated and have merged. Crystal faces can be distinguished in the large particle in the zoomed picture on the right. Scale bar is 100 nm

DEKTAK (4.1.4)

The main result from the DEKTAK measurements were the thicknesses of the silicon nitride and amorphous silicon layers.

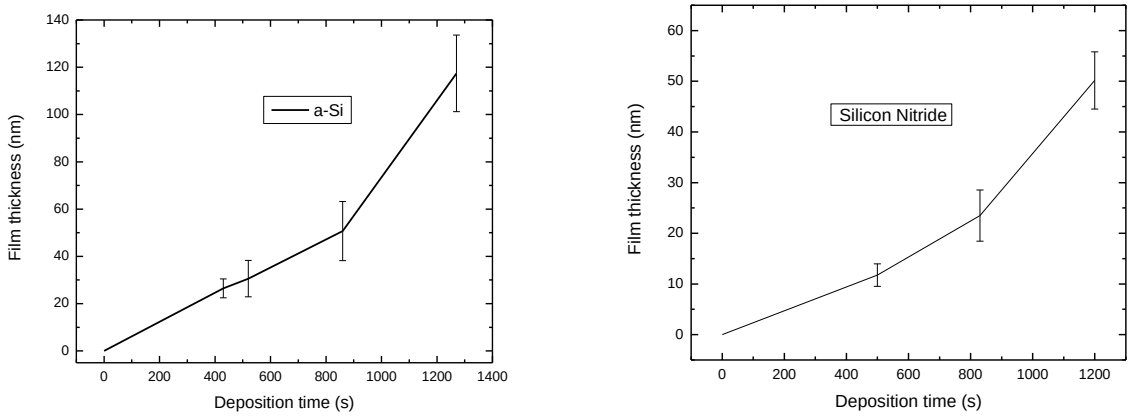

Figure 24. Film thickness versus deposition time for amorphous silicon and silicon nitride.

The amorphous silicon grows much faster than the silicon nitride. This high growth rate may be the reason why the surface of the amorphous silicon shows so many features. All reference samples for the optical measurements have been measured with DEKTAK, except for SS127, the 12 nm amorphous silicon film. This film was too thin to measure using DEKTAK. The 12 nm silicon nitride sample was measured successfully using DEKTAK, as silicon nitride is a much harder material and it had a steeper

edge between the glass and the silicon nitride. Both for amorphous silicon and silicon nitride the growth rate is linear at first and increases for long deposition times.

Raman spectroscopy (4.1.5)

Raman spectroscopy was used to measure the chemical composition of the sample. The aim was to measure the amount of aluminium, presence of aluminium oxide and to confirm the presence/amount of silicon nitride and amorphous silicon.

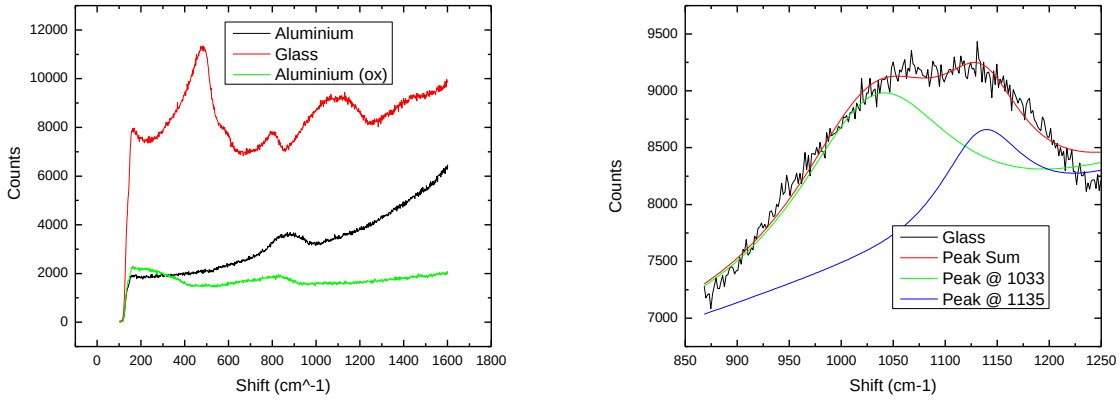

Figure 25. Left: Raman measurements of our glass sample, the aluminium target and a part of the aluminium target with oxidized aluminium, visible as a white dust. Right: the peak in the 900-1250 cm^{-1} range in glass is a convolution of the 1033 and 1135 cm^{-1} peaks.

The peaks in the glass can be recognized clearly. There is a main peak at 480 nm which is associated with silicon bonds. The peak at 810 nm is associated with the O-Si-O bond. The peak in the 900-1250 cm^{-1} range in glass is a convolution of the 1033 and 1135 cm^{-1} peaks.

No.	Material	Type	cm^{-1}	Source	**No.**	Material	Type	cm^{-1}	Source
1	a-Si	TA	150	Zhaoping[13]	**9**	Glass	O-Si-O	810	Malinovsky[14]
2	a-Si	LA	320	Zhaoping	**10**	Glass		1033	Measured
3	a-Si	LO	385	Zhaoping	**11**	Glass		1135	Measured
4	a-Si	TO	480	Zhaoping	**12**	Glass		480	Measured
5	a-Si	2LA	640	Zhaoping	**13**	Glass		565	Measured
6	a-Si	2TO	960	Zhaoping	**14**	Al		860	Measured
7	Si3N4	Si-N	465	Mercaldo[15]	**15**	Al (ox)		830	Measured
8	Si3N4	Si-N	820	Mercaldo	**16**	Al (ox)		165-370	Measured

Table 3. Overview of Raman peaks we expect to measure in our samples based on literature and our measurements of glass and aluminium.

[13] (Zhaoping, 1984)
[14] (Malinovsky, 2000)
[15] (Mercaldo, 2010)

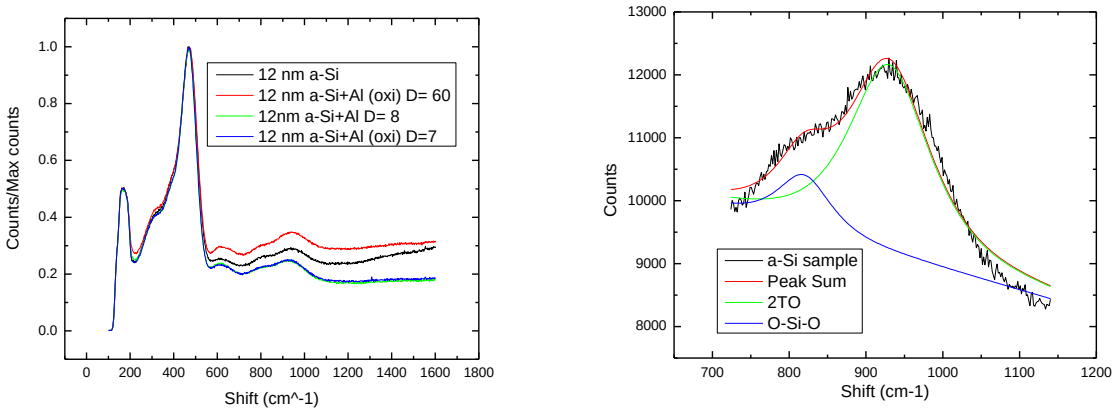

Figure 26. Left: Raman spectrum of a-Si samples with and without particles. D stands for the number of particles per square micron. Ox stands for oxidized particles. Right: the peak in the 700-1050 cm^{-1} range is the convolution of the 2TO and O-Si-O modes.

The amorphous silicon can easily be recognized with a strong TO peak at 480 cm^{-1} which is convoluted with the LO peak at 385 cm^{-1}. The shoulder at 320 cm^{-1} is the LA peak. The next peak is the 2LA peak at 620 cm^{-1}. The graph on the right shows a fit to the final feature, a convolution of the 2TO peak of amorphous silicon and an O-Si-O vibration. The aluminium and aluminium oxide peaks at 860 and 830 cm^{-1} cannot be recognized as the signal in this range is dominated by the 2TO and the O-Si-O vibration modes.

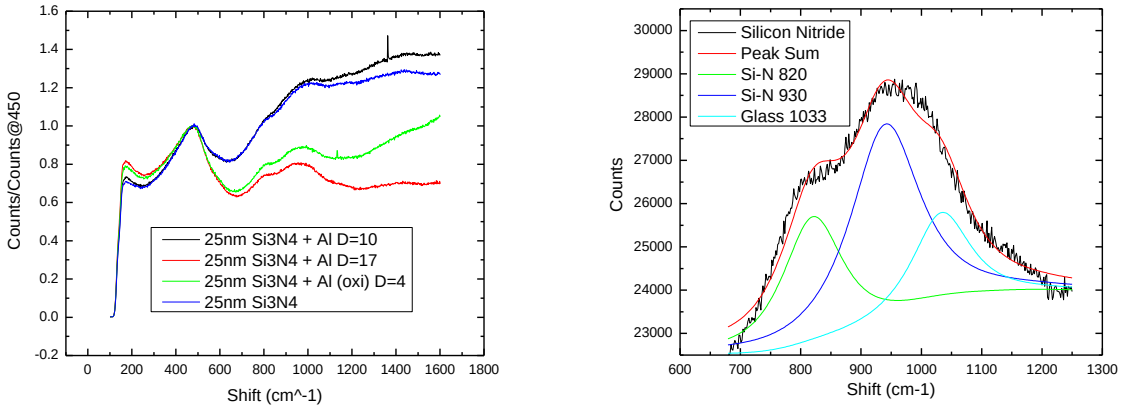

Figure 27. Raman spectrum of silicon nitride samples. D stands for the number of particles per square micron. Ox stands for oxidized particles. Right: the peak in the range of 700 to 1200 cm^{-1} is the convolution of two Si-N peaks and a peak from the glass.

Amorphous silicon nitride features a broad peak around 465 cm^{-1}. The broad peak between 700 and 1200 cm^{-1} consists of the Si-N peak at 820 cm^{-1}, the Si-N mode at 930 cm^{-1} which is twice the main peak at 465 cm^{-1} and a contribution of the 1033 cm^{-1} peak of glass. There could be a contribution of aluminium or aluminium oxide hidden but these three peaks dominate the spectrum in this range. A large fluorescence background can be distinguished in two of the silicon nitride spectra. Although aluminium has a strong fluorescence in the Raman spectrum at 860 cm^{-1} it is difficult to correlate the aluminium particles and the presence of this background in the Raman spectrum because the glass could also be the source of the fluorescence background signal.

Optical properties (4.2)

Predictions (4.2.1)

The optical properties were measured using the Agilent Cary 5000 UV-VIS-NIR Spectroscope. The total reflection (specular plus diffuse), the transmission and the diffuse reflection were measured. From the reflection and transmission the absorption can be calculated. The diffuse reflection is important because the ultimate goal is to create nanoparticles which scatter incoming light. Since the particles are very small the particles are expected have much higher absorption than scattering.

The optical effects are expected to be small. For example, with a particle density of +- 15 per square micron and a typical particle diameter of 12 nm, the surface coverage is only 0.17 percent. If the extinction cross section is 5 times the geometric cross section any effect will be in the order of 1 percent. This is small but it is measurable and it is larger than the uncertainty in the measurements.

FDTD simulations (4.2.2)

Finite differential time domain simulations were run using Lumerical FDTD software. The primary purpose was to predict the wavelength where scattering and absorption occur and to predict the absorption and scattering cross sections of the aluminium nanoclusters. To account for the morphology the results with an aluminium particle covered with Si_3N_4 or a-Si were compared with an aluminium oxide particle in the same configuration. The effect of the particle size, surrounding dielectric and layer thickness were studied.

The following graph, figure 28, shows the relation between the layer thickness and the absorption and scattering cross section for Si_3N_4.

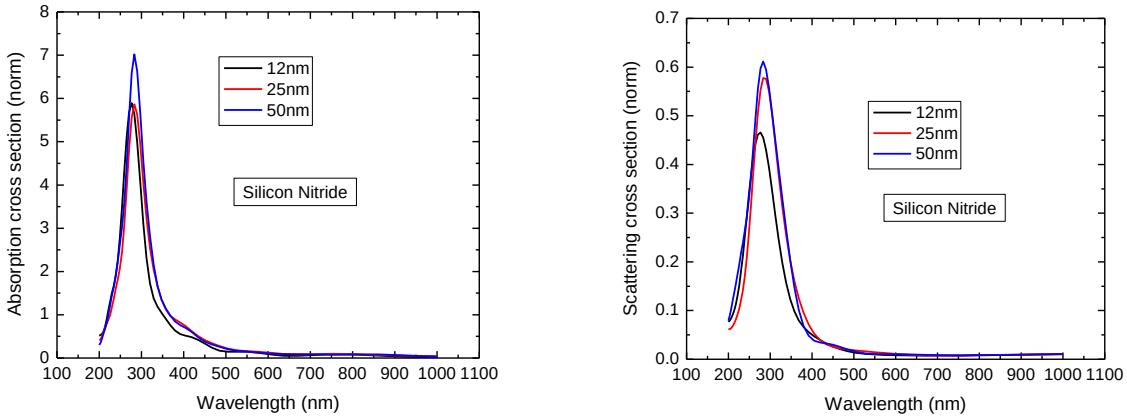

Figure 28. Absorption (left) and scattering (right) cross sections for aluminium particles embedded in Si_3N_4 as a function of layer thickness. Cross sections have been normalized to the geometric cross section of the particle. The peak position is not strongly dependent on the layer thickness. The absorption cross section is about ten times larger than the scattering cross section.

These results show that for these small particles the absorption will be dominant. The absorption cross section is expressed in terms of the geometric cross section of $2.01062 \cdot 10^{-16}$ nm^2 for particles with a radius of 8nm. For a sample with 10 particles per square micron this means that the absorption of the nanoparticles is about 1.4 percent.

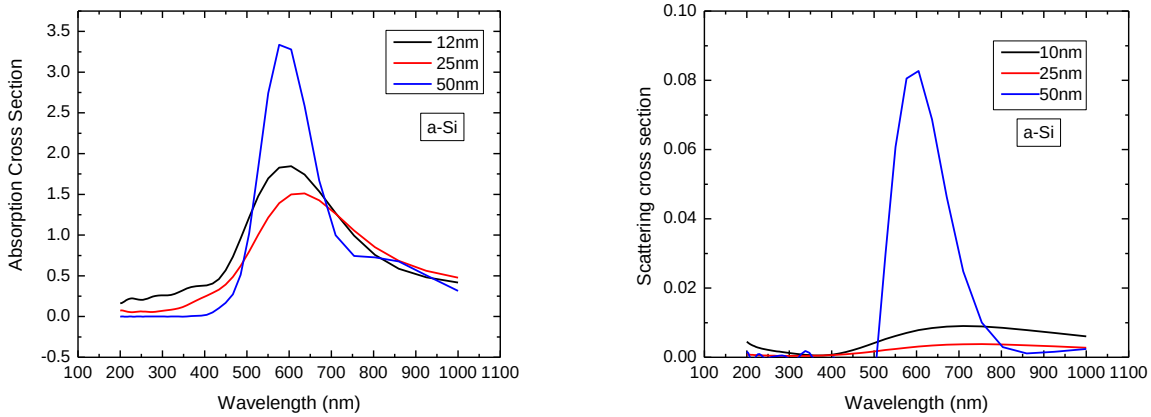

Figure 29. Absorption (left) and scattering (right) cross sections for aluminium particles embedded in a-Si as a function of layer thickness. The absorption is again much stronger than the scattering. This time the absorption and scattering increase when the layer becomes thick. Especially the scattering cross section depends on the layer thickness.

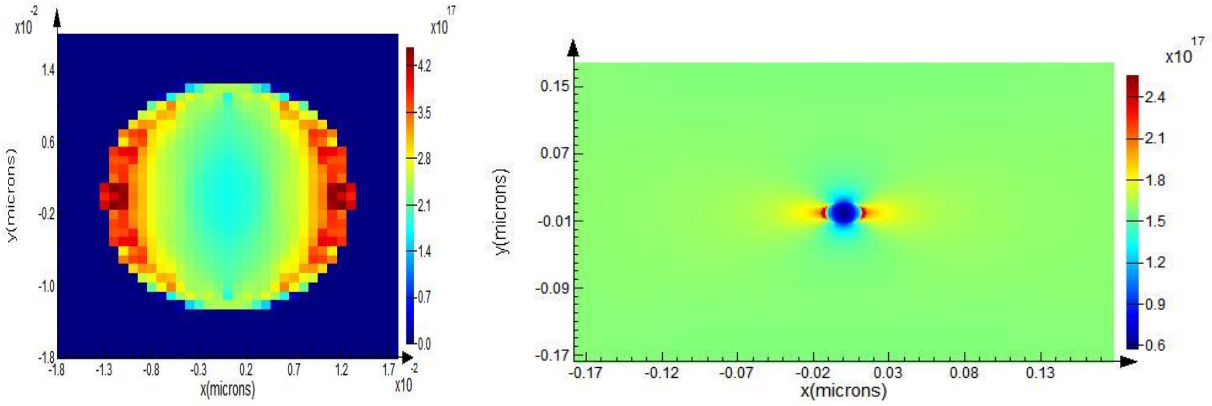

Figure 30. Top (XY) view of the spatial absorption profile around the particle. Spatial absorption is not spherically symmetric because the incident wave is polarized along the X-axis. The field is greatly enhanced in a small area around the particle.

Schottky layer (4.2.2.1)

There is an effect which is not accounted for in these simulations: the transfer of carriers from the silicon to the aluminium nanoparticle due to the difference in the Fermi level. This effect has been studied for silver nanoparticles by F. Huizinga in his thesis and he used the approach by Zhdanov (Zhdanov, 2002) and Ionannides & Verikios (Verikios, 1996). The extra charge on the particles causes a blue shift of the plasmon resonance. To calculate the effect we use the same approach as Huizinga.

For the number of electrons in the sphere we have the following equation:

$$N_a = \frac{4}{3}\pi r^3 * \frac{\rho}{u} A_0 N_{val} = 1{,}29 * 10^5 \qquad 5.1$$

r is the particle radius: 8nm
A_0 is Avogadro's number
*P is the density of aluminium: 2,70 g*cm^{-3}*
u is the atomic weight: 26.9815
N_{val} is the number of conduction electrons per atom: 1

For the total width W, for W >> r we have:

$$W = L + r = \sqrt[3]{\frac{3\epsilon_s r V_0}{e N_d}} + r = 61{,}4 * 10^{-9} m \qquad \text{(Zhdanov, 2002) 5.2}$$

L is the depletion length
*ϵ_s is the permittivity of a-Si, 1,036*10^{-10} F/m*
V_o is the barrier height: 0,55 eV for a-Si and aluminium
e is the electron charge
*N_d is the number of donors, typically 5.6*10^{22} m^{-3}*

From here we can calculate the number of electrons transferred:

$$N_e = \frac{4\pi N_d}{3} * (W^3 - r^3) = 54 \qquad \text{(Verikios, 1996) 5.3}$$

The transferred electrons shift the plasmon resonance according to:

$$\omega_p = \sqrt{\frac{N*e^2}{m_0*\varepsilon_0}} = \sqrt{\frac{(N_a+N_c)*e^2}{m_0*\varepsilon_0}} = 1{,}2748 * 10^{16} \qquad \text{(Verikios, 1996) 5.4}$$

where N_a and N_c are the densities of conduction electrons and additional transferred electrons
*m_0 is the effective mass of the electrons: 1,18 * m_e*
*ε_0 is the permittivity of vacuum: 8,854*10^{-12} F/m*

The peak of the plasmon resonance surrounded by a dielectric is given by the following function:

$$\lambda_{peak} = \frac{2\pi c\sqrt{\varepsilon_m+2\varepsilon_{si}}}{\omega_p} = 5.27 * 10^{-7} m \qquad \text{(Mulvaney, 2001) 5.5}$$

where c is the speed of light
ε_m is the high frequency dielectric constant of the metal: 1
ε_{Si} is the dielectric constant of the silicon: 11,7

This result is obtained assuming the transferred electrons spread uniformly over the volume of the sphere. We know that this is not the case and excess charge will be at the surface of the particle. If we assume that the charge is located in a 1 nm[16] thick layer at the edge of the particle the 54 transferred electrons are in a volume of 7,079*10^{-25} m^3 compared to 2,14*10^{-24} m^3 for the sphere. This increases N_c and increases ω_p which results in a stronger blue shift. This approach has some merit because the plasmon resonance of a metal nanoparticle is a surface phenomenon. The results are given in table 4:

	ω_p *(rad/s)*	λ_{peak} (nm)
no charge transferred	1,2745*10^{16}	526
charge in sphere	1,2748*10^{16}	527
charge in outer shell	1,3854*10^{16}	485

Table 2. Shift in plasmon resonance peak position due to extra charge because of the difference in work function between aluminium and amorphous silicon

So if the charge is on the surface and if this can be accounted for by adjusting N_c in this way there is a significant blue shift due to the charge transferred onto the metal particle. It should be noted that this approach is for metal particles with n-type doping and there is no rigorous theory for the Schottky layer of metal nanoparticles surrounded by intrinsic silicon. The results are sensitive to the choice of N_d which is not properly defined for an intrinsic layer. However, these results show that the blue shift caused by the surface charge that is a result of the Schottky layer can be significant.

So far we have looked at the plasmon resonance of the metal cluster. There will also be an effect on the optical properties of the surrounding silicon. The depletion can be compared to p-type doping, with a p-dopant concentration of 5,5816*10^{22} m^{-3} or 5,5816*10^{16} cm^{-3} in a layer of 53,4 nm around the 8 nm aluminium particle. The effect has been simulated with Lumerical FDTD where a cylinder of 53,4 nm was placed around the particle. The real and complex permittivity of the boron-doped amorphous silicon were taken from (Rantzer, 2001). In this article the dielectric function is given for boron doped amorphous silicon with a concentration that is an order of magnitude greater than we predict in the Schottky layer. The amorphous silicon layer thickness was 25 nm.

[16] (Rouhani, 1973)

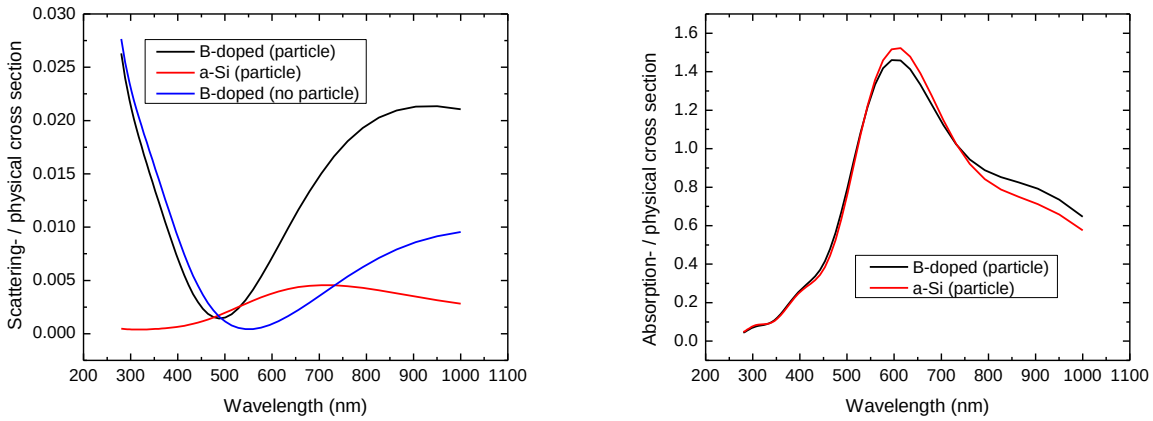

Figure 31. Scattering (top left) and absorption (top right) cross sections for aluminium nanoparticle surrounded by boron doped amorphous silicon compared with normal a-Si. A small broadening in the absorption is observed. The scattering is increased, even without the presence of an aluminium nanoparticle. This could be caused by the introduction of a new material boundary between b-doped a-Si and a-Si.

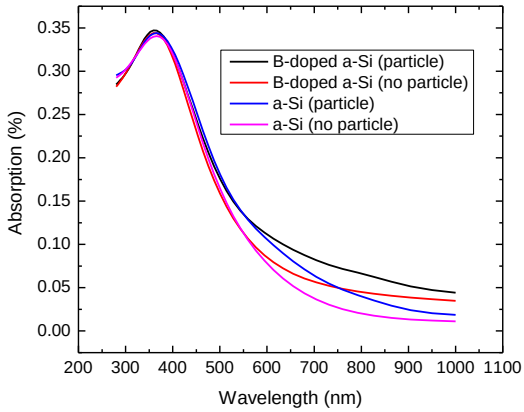

Figure 32. Comparison of absorption in the depletion region around the cluster and the cluster itself. Enhanced absorption is observed above 500 nm. The enhancement is stronger for a cluster surrounded by a disc of boron doped a-Si for wavelengths above 600 nm.

The Schottky layer could cause a slight broadening of the resonance. The extra charge on the particle has a small influence on the plasmon resonance of the particle, causing an 8% shift maximum. A small difference in absorption compared with normal amorphous silicon is caused by the depletion region directly around the particle. For wavelengths between 600 and 1000 nm there is a difference in absorption because of the depletion layer, with a 50 % increase in absorption at 700 nm. The change in optical properties of the material is small but because the field is enhanced in the region directly around the particle, this can still have an effect on the optical absorption.

Size dependent surface scattering (4.2.2.2)

Besides the extrinsic size effect of retardation, there are intrinsic size effects, the most important of which is surface scattering. The aluminium nanoparticles are typically less than 16nm in diameter. The mean free path length in the Drude model for the dielectric function for bulk aluminium is equal to 16 nm (Vollmer, 1995), which is larger than the radius of the particle. This means that the damping term in the equations of motion of the Drude model should be modified to include the effects of surface damping. This results in a modified dielectric function. The FDTD simulations were also run with this modified dielectric function for aluminium. The base dielectric function of aluminium was taken from (Rakić, 1998). The results for a particle with a radius of 8 nm are displayed below in figures 33 and 34:

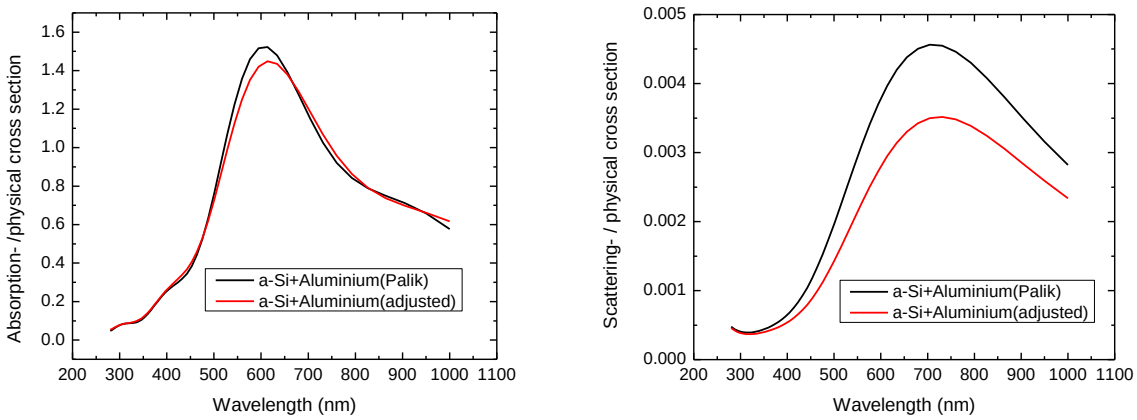

Figure 33. Absorption (left) and scattering cross sections (right) of the aluminium particle with the material data from Palik and the size-adjusted dielectric constant.

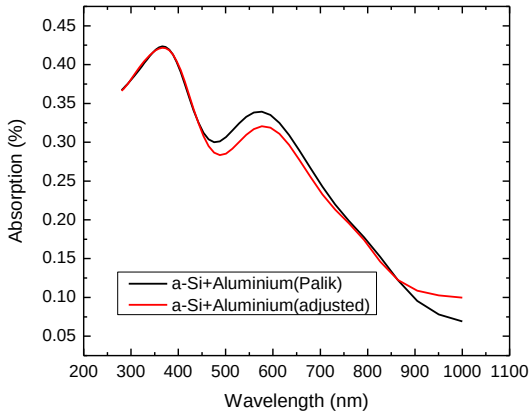

Figure 34. Absorption around the particle with the dielectric function from Palik and the size adjusted dielectric function

The size dependent surface scattering causes a redshift and a slight broadening and weakening of the plasmon resonance, as can be seen from the absorption cross section, scattering cross section and absorption in a 36 nm box around the particle. This effect becomes important when the diameter of the particle is smaller than the bulk mean free path of the electrons, which is around 16 nm for aluminium.

Size dependence (4.2.2.3)

As the particle is very small compared to the wavelength of the incident radiation, the quasistatic limit gives a good approximation for the behaviour of the particle. The FDTD simulations are time-dependent and if there is any extrinsic size dependent effect like retardation, it will affect the outcome of the simulations. As the particle size becomes large compared to the wavelength, the quasistatic approximation breaks down because the field is not constant throughout the particle. In the following graph, figure 35, the effects of particle size, including the size dependent surface scattering, on the scattering and absorption cross section is given for particles embedded in a 50 nm layer of amorphous silicon.

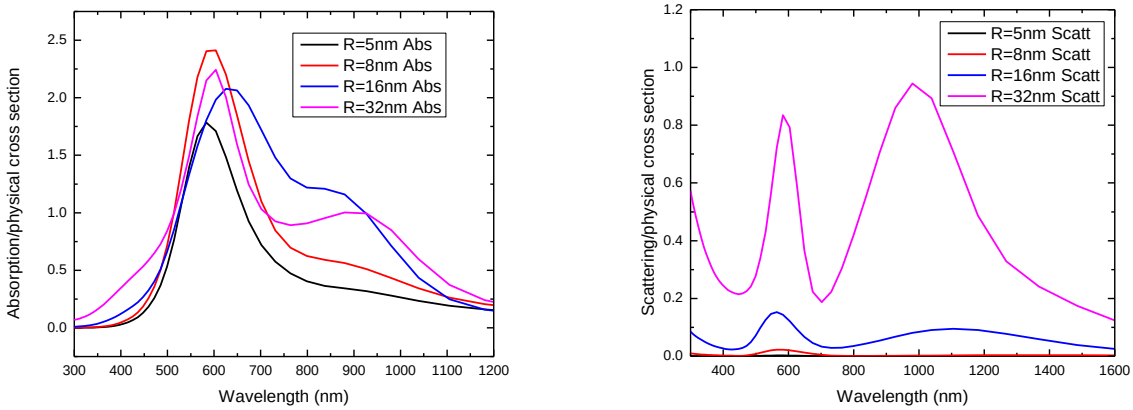

Figure 35. Absorption (left) and scattering (right) cross sections for aluminium nanoparticles embedded in a 50 nm amorphous silicon layer

For large particles, the scattering cross section increases dramatically. The absorption cross section doesn't scale nearly as much with the particle size as the absorption cross section. This is in agreement with theory, which states that the scattering should scale with r^6 and the absorption with r^3. For large particles, multiple modes are observed, whereas for small particles only the dipole mode is observed.

Oxide layer (4.2.2.4)

So far we assumed that there is no oxide layer formed around the particle. After cluster deposition the samples remain in the central chamber for approximately 1 minute before they are brought into the sputter chamber. There background pressure in the central chamber is about $1.1*10^{-5}$ mbar. Because the surface of aluminium is so reactive and the surface to volume ratio of these small metal spheres is so large, it could still be that a small oxide layer is formed on the metal particles. Such an oxide layer would be in the order of 2-5 nm thick[17]. The exact thickness will vary and will depend on the conditions to which the particles are exposed. We simulated the effect of a 3nm thick oxide layer on the absorption and scattering cross sections. Aluminium oxide has a dielectric constant of 9.3, which affects the resonance. The metal core shrinks so the absorption will be smaller compared with a pure metal particle. Size-dependent surface damping also becomes more important as the size of the metal core decreases.

[17] (Akimov&Koh, Design of Plasmonic Nanoparticles for efficient subwavelength light trapping in thin film solar cells, 2011)

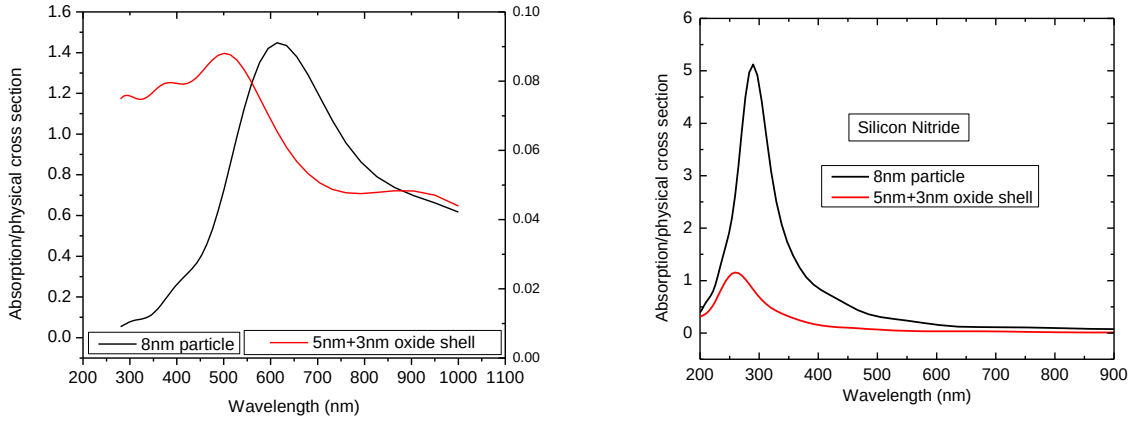

Figure 36. Absorption cross section for the particle with an oxide ring in amorphous silicon (left) and silicon nitride (right). The oxide layer reduces the cross section dramatically, especially in the case of amorphous silicon. The effect of the surface damping is smaller than the effect of the chance in dielectric environment.

Absorption (4.2.2.5)

In order to relate the FDTD simulations with the UV-Vis measurements we need to calculate the absorption per particle. We take the inverse of the particle density, the area per particle, then we compare the absorption of the sample with a 25nm a-Si layer with the absorption of a 25nm a-Si layer with the 8-nm aluminium particle and the depletion region around it. The dielectric function of the aluminium has been adjusted to account for surface damping. The results for amorphous silicon are given in figure 37:

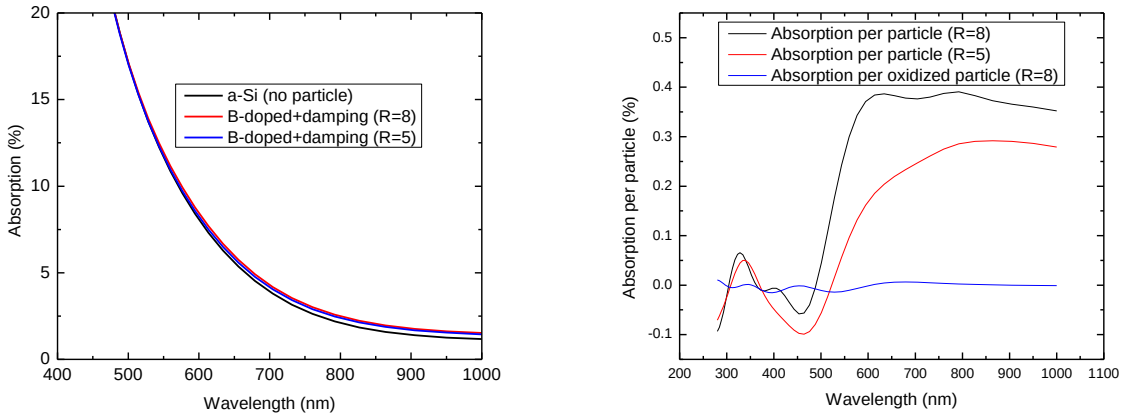

Figure 37. Left: absorption in a 0.35 by 0.35 micron area around the particle (area per particle). Right the change in absorption compared with a plain amorphous silicon layer, per particle.

The increase in absorption is strong near the plasmon resonance peak around 600 nm. The enhancement is much stronger because of the stronger plasmon resonance. We expect an enhancement of optical absorption around 600 nm, in the order of 0.5% per particle. This result was obtained by taking a value for the volume per particle using the particle density and comparing the

absorption in this volume when there is a particle present with the absorption without the particle. The UV-Vis data was analyzed to obtain the absorption per particle.

For silicon nitride the results are displayed in figure 38:

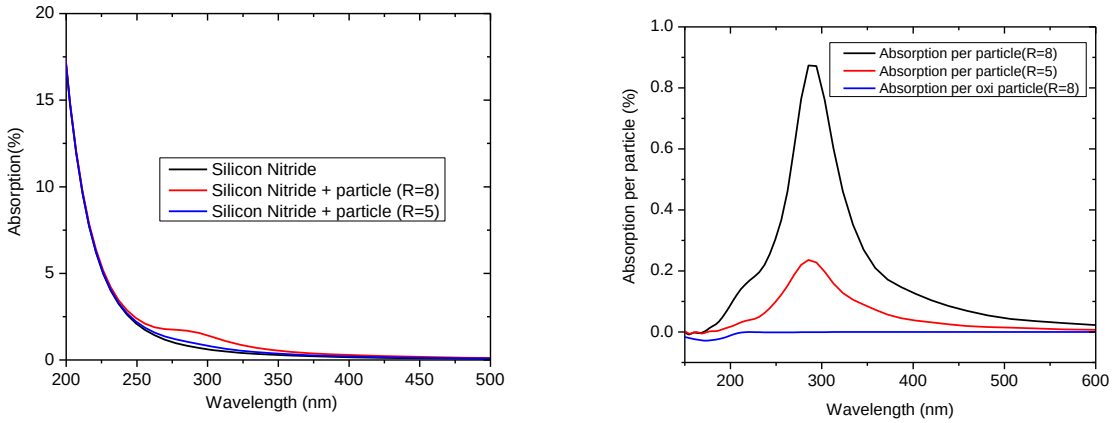

Figure 38. Absorption in a 0.35 by 0.35 micron box around the particle (left) and the change in absorption per particle (right).

We see that in both cases the absorption per particle is in the order of 0.5 to 1%. For amorphous silicon the increase in absorption is purely within the particle itself, for silicon nitride the plasmon resonance is in an energy range where the silicon is optically active and the resonance is broader. The oxidized particle reduces absorption slightly in the frequency range where silicon nitride and silicon start absorbing, around the band gap.

UV-VIS results (4.2.3)

The optical properties of the samples were measured using the Agilent CARY-2000 UV-Vis-NIR spectroscope. We measured the transmission and the diffuse and total reflection (diffuse plus specular). The FDTD simulations gave an indication of where to look for any plasmonics effects and they also indicate that absorption will be the dominant plasmonic effect. The effects of the nanoparticles were not visible with the naked eye. The oxidized particles form a white dust as could be seen in the cluster source itself during cleaning, but there was nothing visible on the glass.

The absorption and scattering of the samples with clusters and a layer were compared with a plain layer of Si_3N_4 or a-Si. The results from the plain layer measurements were subtracted from the results of the samples with clusters to observe the effect of the particles. To account for morphology samples with oxidized aluminium particles and a layer of Si_3N_4 and a-Si were also made. We will compare the results of the aluminium nanoparticles with the oxidized aluminium nanoparticles.

The absorption measurement was also corrected for the particle density. To determine the particle density we used the AFM results of each corresponding sample and of a reference sample with no layer of Si_3N_4 or a-Si. However, the a-Si samples were very rough and it was impossible to distinguish the aluminium nanoparticles under the silicon. Therefore the uncertainty in the a-Si particle density is large (50%).

The glass we used for our depositions also absorbs some of the light. The glass starts absorbing around 380 nm and the absorption peaks at 250nm. This means that for short wavelengths the glass may influence the results, introducing an uncertainty.

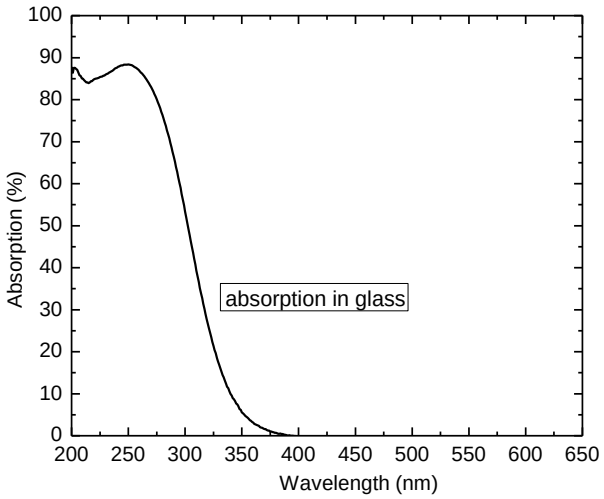

Figure 39. Absorption in glass. Above 380 nm the absorption is virtually zero. At short wavelengths the glass may interfere with our results. Especially for silicon nitride, which should start absorbing in the same wavelength range this needs to be kept in mind.

Results - Si_3N_4 (4.2.3.1)

The results for the absorption of the silicon nitride samples with the glass are displayed in the following graphs, figure 40:

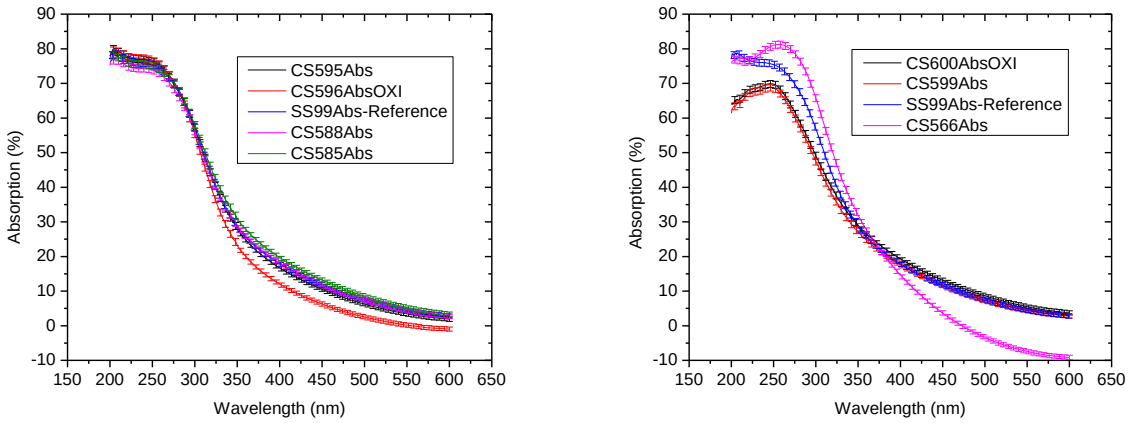

Figure 40. Absorption of Si_3N_4 samples with clusters compared with the reference 25 nm Si_3N_4 layer without clusters: SS99 (in blue). The absorption of the silicon nitride increases slowly between 600 and 350 nm, between 350 and 275 nm it increases sharply because of the glass and below that it levels off. The results of CS566, CS599 and CS600 in the graph on the right are diverging from the other samples. The absorption of CS566 is negative for large wavelengths, this is a clear error.

We are looking for the effect of the particles, so the results from the reference sample are subtracted from the samples with particles. In the figure 41 the absorption is compared with the absorption of the reference 25nm silicon nitride sample, SS99. Note that the absorption has been determined by measuring the transmission and reflection. In the following section the difference in absorption between the samples and the reference sample is discussed.

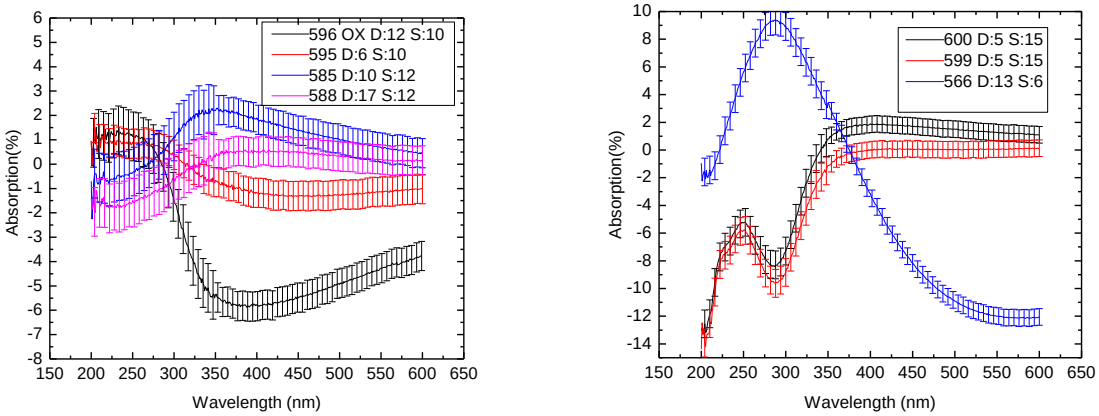

Figure 41. Absorption of the silicon nitride samples compared with the reference, SS99. 'D' stands for the particle density (per square micron) 'S' stands for the particle diameter.

The results for the samples with a 25 nm silicon nitride layer have been divided into two groups. The main group is the one in the graph on the left. The samples in the graph on the right had a very low particle density (CS600, CS599 at 4 per square micron) or the results were unreliable as is the case for CS566 where the absorption is -10% at 600 nm. Therefore we focus on the samples in the left graph.

It is clear that the particles have a significant effect on the optical absorption. The three samples with unoxidized nanoparticles all have an increased absorption either at 250 nm or around 350 nm. The oxidized sample, CS596 clearly has an opposite trend with a decrease in absorption around 350 nm and like CS585 and CS588 it is a broad dip. The absorption of the sample with the oxidized particles compared with the reference sample increases at short wavelengths around 250 nm.

The fact that the effect is significant and the fact that the effect of the metal particles is opposite to the oxidized nanoparticles is encouraging as it means that the enhanced absorption of the samples with aluminium nanoparticles in not just caused by a morphological effect but by the metal/oxide.

The peak position of CS585 is at 350 nm, the peak of CS588 and the sample with oxidized nanoparticles CS596 is at 375 nm. Although CS588 has a higher particle density than CS585, the effect on the absorption is smaller. For CS588 the decrease in absorption at short wavelengths bigger than the decrease in CS588. CS595 has a low particle density which makes its results less reliable. However, while CS588 and CS585 have a decrease in absorption from 200 to 275 nm, CS595 has increased absorption compared to the reference at these wavelengths.

In order to quantify the effect of the particles we need to take the particle density into account. There is a large uncertainty in the particle density, because it is based on AFM measurements and the density can change depending on the part of the sample that is measured. Most of the error originates from the uncertainty in the particle density.

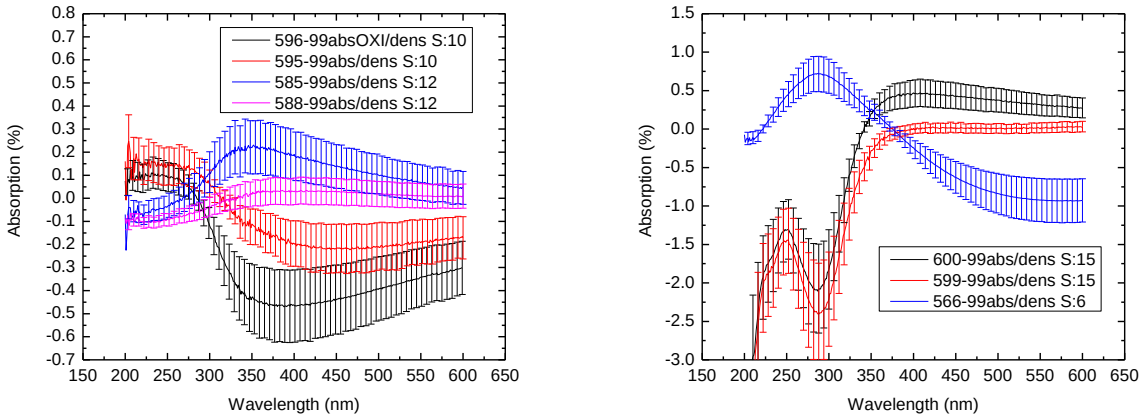

Figure 42. Absorption minus the absorption of the reference sample, divided by the particle density. 'S' stands for the typical particle diameter. CS596 and CS600 are oxidized. There is no significant difference between CS599 and CS600. The trend between CS595 and CS596 is also similar. It is clear that samples that have been made in quick succession have similar absorption profiles.

In figure 42 the difference between the absorption and the absorption in the reference sample has been adjusted for the particle density. Because the particle density is difficult to determine there is an additional contribution to the uncertainty. However, the trends become more apparent. The oxidized sample CS596 has the same trend as a sample with particles that are not oxidized; CS596. Samples which have been made in quick succession have a similar effect on the absorption per particle. This makes sense because the samples that are made in one batch are more likely to have a similar particle density and size distribution.

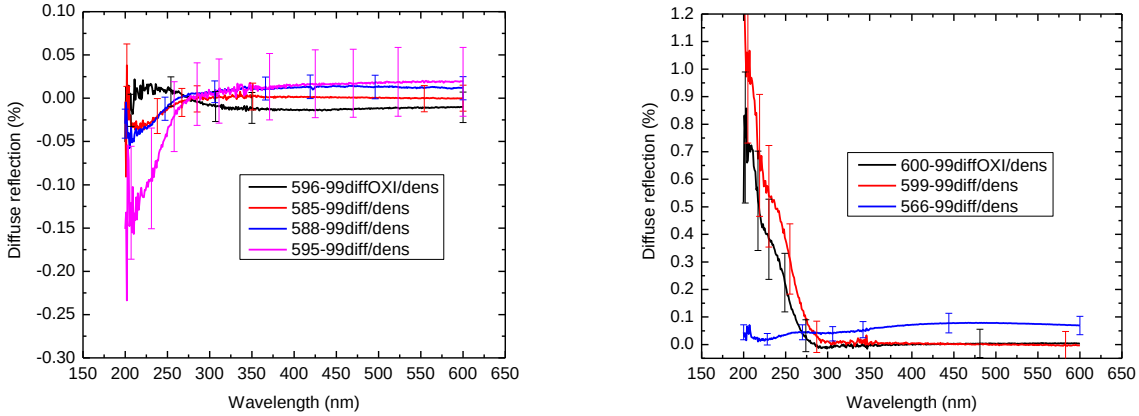

Figure 43. Diffuse reflection of the 25 nm Si3N4 samples, compared with the reference sample.

The results of the diffuse reflection measurements do not give as much insight as the absorption measurements. For these small clusters any plasmonic effect on the absorption will be a lot stronger than on the scattering. The measurement error is also increased, especially at short wavelengths because the electronic gain factors of the equipment are increased as the signal becomes very weak. What makes these results interesting is that there is an effect at wavelengths below 275 nm and the effect of the oxidized particles is opposite to the effect of the aluminium nanoparticles. The decrease in scattering could be caused by absorption in the metal particle, the increase by the induced surface roughness of the particles underneath.

Results – a-Si (4.2.3.2)

Samples with aluminium particles covered with 12, 25 and 50 nm layers of a-Si. The transmission and reflection were measured and compared with the reference samples. Unfortunately it was very difficult to determine the particle density, which increases the uncertainty for the density adjusted absorption.

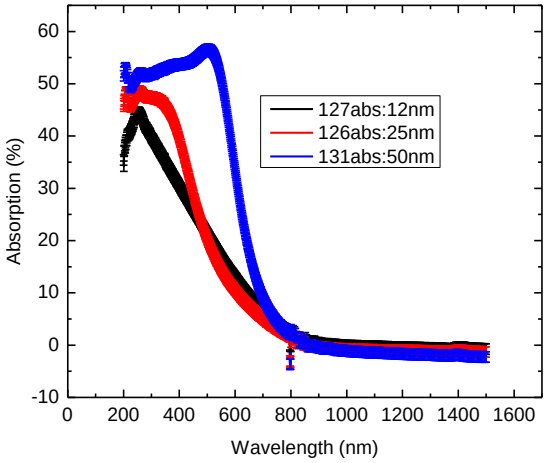

Figure 44. Absorption of the reference a-Si samples. The blue curve of the thickest layer of a-Si on glass is the most similar to bulk a-Si.

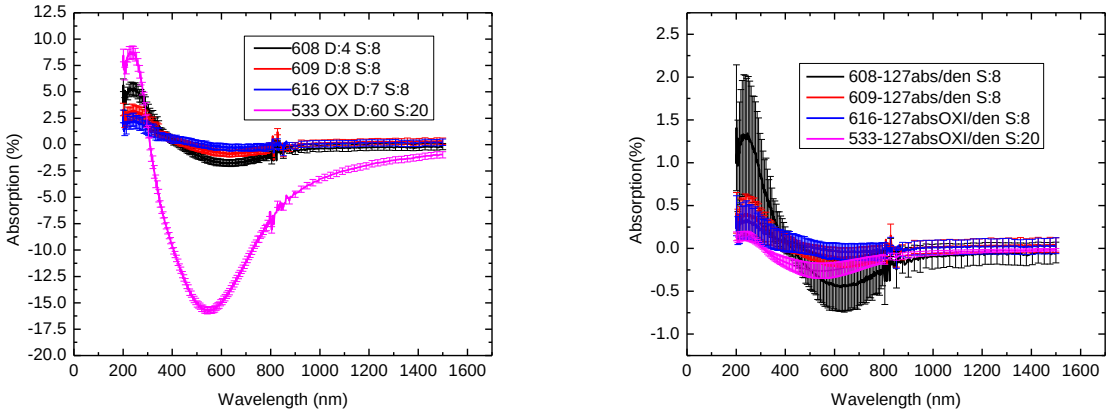

Figure 45. Left: Absorption for the 12nm a-Si samples compared with the reference 12 nm a-Si sample. 'D' stands for the particle density, 'S' for the average particle diameter. Right: absorption compared with reference divided by the particle density.

The curves above in figure 45 show the absorption of the samples with aluminium nanoparticles compared with the reference 12 nm a-Si sample. The shape of the curves is similar to the shape of CS596, the sample with oxidized particles in 12 nm Si_3N_4, with a decreased absorption around 600 nm and an increased absorption at short wavelengths. The increase in absorption may be erroneous because the absorption curve of the reference sample SS127 shows an unusual dip below 275nm. This is where the glass also affects the optical absorption.

Focusing on the decreased absorption around 600 nm we notice that the effect is the same for the oxidized and the non-oxidized samples. CS533, the sample with the extremely high particle density and large particles has a much stronger effect and the peak wavelength is shifted at 550 nm compared with 600 nm for the other samples. Looking at the absorption per particle, the effect is almost the same in magnitude for each sample, in the order of 0,5%. We can conclude that there is no noticeable difference between oxidized and non-oxidized particles in this sample. The sample with a high particle density (CS533) features oxidized particles and when corrected for the particle density, the results match the other oxidized sample (CS616) very well.

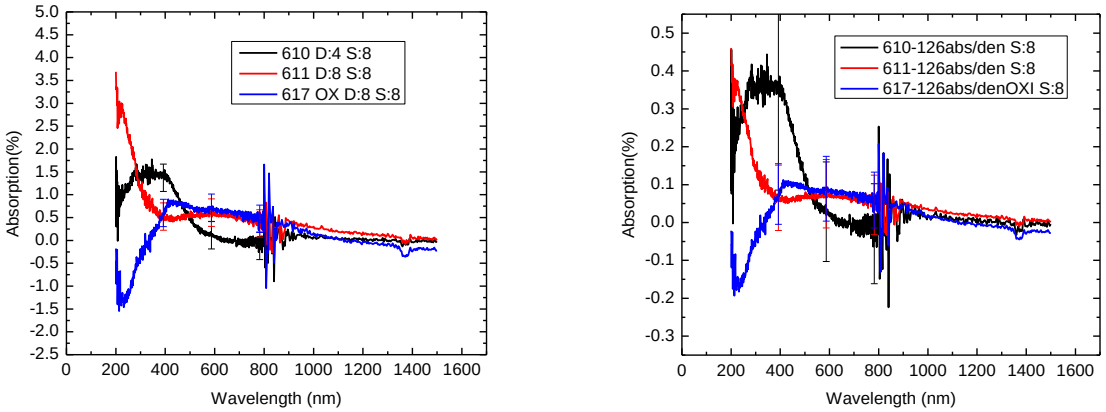

Figure 46. Absorption in 25-nm a-Si compared with the reference (left) and adjusted for the particle density (right). The noise at 800 nm is caused by electronic gain; the signal is weak because only a small fraction of the light passes the grating. This is the first batch with slightly higher densities and larger particles than CS615 and CS618.

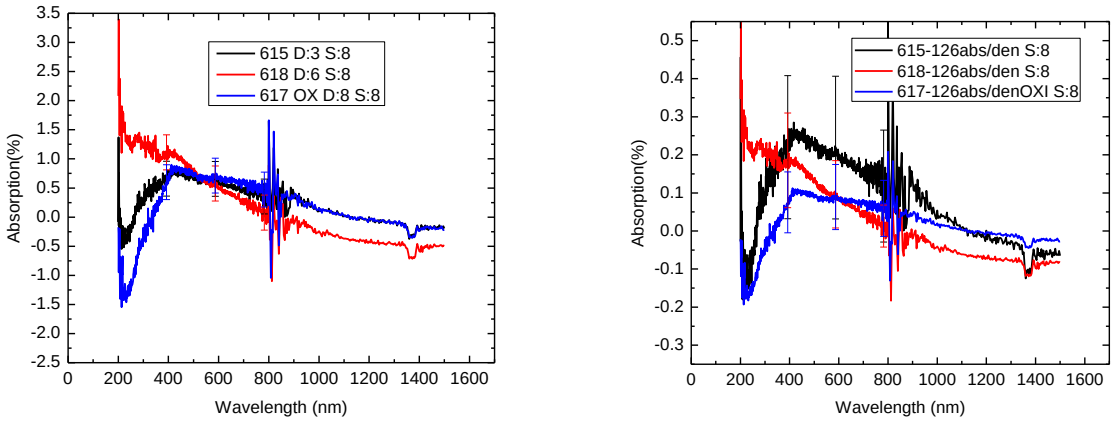

Figure 47. Absorption in 25 nm a-Si compared with the reference and adjusted for the particle density (right). This is the second batch with slightly smaller particles with a lower density.

The results of the 25 nm a-Si samples show a mixed picture. In the first batch (figure 46) both of the samples with aluminium nanoparticles have increased absorption at short wavelengths whereas the sample with oxidized particles has a decrease in absorption. Sample CS 615 of the second batch (figure 47) has a different trend, CS618 has an increase in absorption like the other samples but CS615 shows a decrease. However, CS 615 is the sample with the lowest particle density and the smallest particles out of all the samples we studied, which therefore can be ignored further.

In the first batch, adjusting for the particle density does not change the trend of the curves. In the second batch adjusting for the particle density makes it appear as if there is a peak for CS615 compared with the sample with oxidized particles, CS617. Because there is no such peak present in the absorption results before taking particle density into account and because the particle density is so uncertain.

At higher wavelengths there is noise at 800 nm and a dip around 1400 nm. The noise is caused by electronic gain and the dip is caused by absorption in the lens.

To summarize, there is slightly increased absorption at wavelengths below 400 nm for the aluminium nanoparticles and there is a decrease in absorption with oxidized nanoparticles at these short wavelengths. There is no dip in the absorption around 600 nm, as is the case for the 12 nm and the 50 nm a-Si samples. A metallic effect is observed, at shorter wavelengths than was expected.

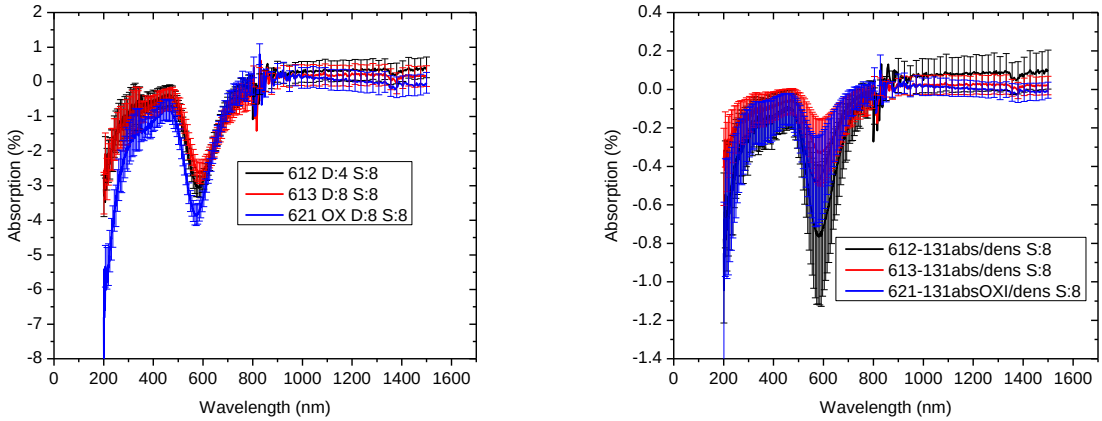

Figure 48. Absorption for 50 nm a-Si. The absorption is again compared with the absorption in the reference sample (left) and then adjusted for the particle density (right).

The results for the 50 nm a-Si samples are shown in figure 48. The results are similar to the 12-nm a-Si samples, with a dip around 600 nm. This dip is right where the amorphous silicon starts absorbing. That means that in this wavelength range a reduction in the thickness of the amorphous silicon layer or the introduction of holes has a strong effect on the absorption. The effect adjusted for particle density is also in the same order of magnitude, below 1%. However, where the 12 nm samples with particles have increased absorption compared with their reference below 300 nm, the 50 nm samples with particles have decreased absorption in this wavelength range.

The results for 12 and 50 nm a-Si are similar with a decrease in absorption around 600 nm, both for the aluminium nanoparticles. The dip width is similar between these two and the effect per particle is also similar, considering the wide error margin in the particle density. The samples with a 25-nm a-Si layer have very different results. Here, there is almost no effect in the 400-800 nm range but there is an increase in absorption below 300 nm for the samples with aluminium particles and a decrease for the samples with oxidized particles.

The diffuse reflection of the a-Si samples was also measured. However, the diffuse reflection was effectively zero for all samples within the range of 200-1400 nm.

Optical measurements and FDTD results: comparison (4.2.4)

The results of the FDTD simulations are used to interpret the results of the optical measurements. We compare the results of the FDTD simulations with the optical measurements and with theory.

Silicon Nitride (4.2.4.1)

When particles are embedded in silicon nitride the plasmon resonance of the particles shifts to about 300 nm. The scattering cross section is much larger than the absorption cross section for these small particles. This is in agreement with theory. The order of magnitude of the absorption per particle compared to the reference is comparable with the measurements of the 25 nm silicon nitride layer at 0.5%. Neither the wavelength nor the magnitude of the resonance are strong functions of the thickness of the silicon nitride layer. The scattering is very weak compared with the absorption, this is in agreement with theory and the optical measurements.

The absorption per oxidized particle is not in agreement with the FDTD simulations. In the FDTD simulations there is a slight reduction in absorption of about 0.025% around 300 nm. This is where the silicon nitride in the simulation starts absorbing. The effect of the oxidized particles is much larger than expected, with a reduction of 0.5% around 400 nm. This could have multiple causes. First of all the amount of oxidized matter may be underestimated. The densities we worked with are the densities of particles with a size of more than 4 nm, for which plasmonic interactions are expected. There is also a large tail of smaller particles with a size of 1-4 nm. These particles are difficult to detect with the AFM and are impossible to detect once a silicon nitride layer is added. These particles could reduce the absorption when they are oxidized. Also, the silicon nitride layer that is formed on the oxidized particles may not form a fully closed cover. This means that there are vertical optical holes in the material where large oxidized particles are located. This can also reduce absorption.

Although the magnitude of the enhanced absorption for the metallic particles is in agreement with the simulations, the wavelength is not. The FDTD simulations predict enhanced absorption around 300 nm, while we observe enhanced absorption around 400 nm. The absorption data for the silicon nitride layer is also not in agreement with the simulations.

The FDTD simulations use data for the dielectric function of amorphous silicon nitride from Philipp[18]. Data on the optical properties of α-silicon nitride was also taken from Xu & Ching[19]. This data was a good match with the data from Philipp, but not with our optical measurements. Perhaps a small amount of excess silicon is the cause of the reduction in the band gap[20]. For amorphous materials the growth conditions can affect the structure and therefore the optical properties. If the optical properties of silicon nitride in the simulation is wrong this also explains why the increase in absorption due to the plasmon resonance of the aluminium particles is observed at 350 nm while the simulations suggest it should be at 300 nm. We also did not consider any possible effects of a charge transfer in the interface between silicon nitride and the metal particle.

The peak is also broader than the FDTD simulations predict. This is explained by the fact that we have an ensemble of particles with different sizes and by the fact that our simulations neglect chemical interface damping. The resonance is also shifted further than was expected based on the simulations. These effects all broaden the resonance.

Amorphous silicon (4.2.4.2)

With amorphous silicon, no plasmon resonance is observed at the wavelength where it was expected. We did observe a metallic effect at short wavelengths, under 400 nm. The simulations suggested that there is a plasmon resonance around 600 nm. The magnitude and the position of the resonance do not depend strongly on the layer thickness according to the simulations. The optical properties of amorphous silicon used in the simulations are in good agreement with the optical measurements. The increase in absorption per particle is in the order of 0.5% according to the simulations. There is also a slight reduction in absorption around 600 nm for an oxidized particle.

In our optical measurements indeed no scattering is observed, as expected from theory and simulations. The reduction in absorption for oxidized particles was observed. As with silicon nitride, the effect of the oxidized particles on the absorption was the largest around the band gap at near 600 nm. For wavelengths longer than 600 nm the silicon is not absorbing, so any optical holes in the material do not affect the absorption; for wavelengths for below 600 nm the silicon absorbs so much that small holes do not matter. Only for intermediate wavelengths around the band gap the oxidized particles have a large impact on the absorption. This explains the effect of the oxidized particles on the absorption of silicon nitride and amorphous silicon. The magnitude of the effect is again larger than the FDTD simulations suggest, this has the same explanation as with silicon nitride: there is a tail of small particles in the distribution which are impossible to measure using AFM and the silicon may not grow conformally on the oxidized particles, leaving optical holes in the material.

With amorphous silicon the particle size and density was small. Unfortunately we were not able to measure the particle density of the samples with amorphous silicon because the amorphous silicon was too rough to be able to distinguish the metal nanoparticles.

[18] (Philipp, 1973)
[19] (Xu&Ching, 1995)
[20] (Deshpande, 1995)& (Aspnes&Theeten, 1979)

A metallic effect was observed at short wavelengths, below 400 nm, for the samples with a 25 nm layer of a-Si (figures 46 and 47). In this wavelength range the uncertainty is large because the glass is absorbing and the amorphous silicon is also absorbing. However, there is a clear difference between the absorption of the best samples of the two batches (CS611 and CS618) and the sample with oxidized particles and the effect is bigger than the uncertainty in the measurements. The effect per particle is comparable in magnitude with the results from silicon nitride (0.2%). What makes these results hard to interpret is that the shape of the absorption peak is different for both these samples. The shape is even different for two samples with the same cluster deposition parameters (CS610 and CS611) but different deposition times. This suggests that this metallic effect depends strongly on the deposition parameters.

FDTD simulations and theory suggested that the plasmon resonance peak is shifted to around 600 nm but is also significantly broadened compared with the plasmon absorption peak of the particle in silicon nitride. The combined effect of the broadened peak and the low density of small particles in our samples with amorphous silicon can explain why no plasmon resonance is observed at 600 nm.

This does not explain why there is a metallic effect observed at shorter wavelengths (300-400 nm). If it is a broad plasmon resonance that causes the increased absorption at short wavelengths, the change in dielectric environment of the metallic particles does not shift the resonance as was expected. Perhaps the amorphous silicon does not grow conformally around the particle. It could also be that the FDTD simulations were not correct and the aluminium nanoparticles need to be in between two layers of amorphous silicon to shift the plasmon resonance to higher wavelengths. Although it wasn't observed with the silicon nitride samples, the formation of a small oxide layer around the particle could also blue-shift the resonance compared with a purely metallic particle in amorphous silicon. There are additional effects such as chemical interface damping, described by Kreibig and Vollmer, which could shift the resonance. For these very small particles (<10nm), the surface is relatively large compared with the volume and surface effects will have a stronger influence on the optical properties compared with the slightly larger particles of the silicon nitride samples.

Discussion (5)

For silicon nitride, an increase in the absorption was found around 350 nm with metallic nanoparticles. With amorphous silicon, a small increase in absorption was observed at wavelengths below 400 nm.

Uncertainties (5.1)

The largest uncertain factor in this research was the precise composition of the samples. The cluster source is a very unpredictable system which can give different results when using the same or similar settings twice. Clusters with a wide range of sizes are produced and the samples are not deposited uniformly over the surface of the glass. Measuring the density with AFM on one spot of the sample can give different results than another spot just a few millimeters apart. Then the particles are covered with silicon nitride or amorphous silicon which makes then even more difficult, or in the case of amorphous silicon, impossible to detect. This creates the large uncertainty in the particle density. Since the observed effect per particle per square micron is very small (0,5%) a large particle density is necessary for the optical measurements to be reliable.

The measurement error using the Agilent Cary 2000 UV-Vis-NIR spectrophotometer was small compared to the uncertainty in particle density. At short wavelengths under 300 nm the results are less reliable because the baseline measurement is not equal to zero: a black sheet is used for the baseline measurement but it isn't fully absorbing under 300 nm. At the low wavelength end of each source, so under 300 nm and between 900 and 700 nm the amount of light that passes the grating is small so electronic gain is increased to maintain signal strength which creates noise.

The Raman measurements are very accurate. It is unfortunate that aluminium has no sharp peaks that can be distinguished within the background of silicon nitride or amorphous silicon. The aluminium or aluminium oxide could not be measured with Raman spectroscopy and we could not determine the particle density using Raman spectroscopy. The DEKTAK measurements are very accurate but difficult to interpret. It is not always clear where the interface between the glass and the silicon nitride or silicon is. Multiple measurements on multiple places were done with each sample to reduce the error.

The sputter source is a much more consistent system than the cluster source and two samples with the same deposition time will have the same layer thickness. However, when growing a layer over nanoparticles it is not certain how this layer forms. We assume that the layers grow conformally around the spherical particle for our FDTD simulations, creating a shell around the particle. This is a slight simplification as the layer may grow around the sphere to form a Gaussian shaped surface. If the layer does not grow properly around the particle, the film may be thin right above the particle. The AFM images tell us that there is definitely a layer of silicon nitride that grows over the particles but we don't know if the layer maintains a constant thickness when growing over these particles. The pressure in the central chamber is also in the order of 10^{-5} mbar, while the cluster source and sputter chamber have pressures in the order of 10^{-9} mbar. Even though the particles are in the central chamber for a short time, a thin oxide layer could still be formed.

Comparison with previous research (5.2)

Little to no previous work has been done on aluminium nanoparticles embedded in a dielectric. There has been quite some research on silver nanoparticles embedded in silicon nitride and silicon[21], also in the context of solar cells. There has been some work on aluminium nanoparticles in air or vacuum in the context of solar cells, mostly numerical.

Akimov and Koh did a numerical study to find the optimal parameters to enhance absorption in an a-Si:H solar cell using silver and aluminium plasmonic nanoparticles. They found that for aluminium nanoparticles with a radius of 10 nm the enhancement of absorption of light with the AM1.5G spectrum was nearly 20% with a surface coverage of 70%[22]. We do not reach this particle size, let alone these kinds of particle densities. For large particles with a radius of 70 nm, they found that the absorption could be enhanced by 15% with a surface coverage of 12%. We are unable to produce these kinds of particle sizes or densities with the cluster source.

Akimov and Koh pointed out that the higher order resonances of particles may be more suited to enhancement of absorption in solar cells. Indeed we find through our simulations that the quadrupole scattering term, which increases very quickly with increasing particle size, has a larger scattering to absorption cross section than the dipole term. However, this resonance is shifter out of the desired range when the particle is embedded in amorphous silicon. It is worth investigating if the higher order modes can be shifted into a wavelength where they can contribute to optical absorption.

[21] (Xu, 2003), (Mertens, 2004), (Beck, 2009)

[22] (Akimov&Koh, Resonant and nonresonant plasmonic nanoparticle enhancement for thin-film solar cells, 2010)

Conclusion (6)

Samples with aluminium nanoparticles on glass covered with silicon nitride and amorphous silicon have been made. Typical average particle size was 10 nm in diameter and a typical density was 10 particles per square micron. With a 25 nm layer of silicon nitride we were able to observe the particles with AFM, the amorphous silicon was too rough to observe the particles directly. TEM imaging confirmed the presence of particles in a sheet of amorphous silicon for one sample and confirmed that the size and density were in agreement with those deduced from the AFM images. Raman spectroscopy was used and this confirmed the composition of the sample but the peaks of aluminium oxide and aluminium were not distinguishable under the signal of amorphous silicon and silicon nitride.

Optical measurements of the samples with aluminium nanoparticles embedded in a 25 nm layer of silicon nitride showed an increase in absorption with a broad peak around 350 nm. The increase in absorption per particle was 0.25% for one sample. This is in reasonable agreement with the FDTD simulations, where an increase in the absorption of about 0.5% was predicted at 300 nm. The difference in wavelength can be explained by the difference between the optical properties of our silicon nitride and the properties reported in literature which were used for the FDTD simulations. The broadening of the peak compared with the simulations can be explained by the fact that the resonance is shifted further than the FDTD simulations predicted and that we have an ensemble of particles. We successfully made aluminium nanoparticles deposited on glass, embedded in amorphous silicon and silicon nitride and were able to observe the nanoparticles in silicon nitride using AFM. We showed that the aluminium nanoparticles embedded in silicon nitride enhance absorption and compared this with plain silicon nitride layers and with oxidized aluminium nanoparticles embedded in silicon nitride. Our optical results were in reasonable agreement with FDTD simulations.

Optical measurements of aluminium particles embedded in amorphous silicon showed a reduction of absorption with oxidized particles, as expected, but no increase with metallic nanoparticles. This can be explained by the low density of particles and the small particle sizes. Also, the peak is broadened more than with silicon nitride because of the bigger resonance shift. No plasmon resonance was observed at the expected wavelength, around 600 nm. We did observe an increase in optical absorption around 300-400 nm with metallic particles compared with oxidized particles for the amorphous silicon samples with a thickness of 25 nm. This could be a plasmonic effect, if the growth of the amorphous silicon around the particles was imperfect, or if a small oxide layer is formed, or if the FDTD simulations were not correct and the particles need to be embedded between two layers of amorphous silicon to shift the resonance further. In any case, both with silicon nitride and amorphous silicon an effect of the aluminium clusters on the optical absorption was observed which was not just a morphological effect but caused by the metal nanoparticles. In both silicon nitride and amorphous silicon, the optical absorption increased with metallic aluminium particles and decreased with oxidized aluminium particles.

Recommendations (6.1)

The system of aluminium nanoparticles embedded in silicon nitride and amorphous silicon has successfully been made using the gas aggregation cluster source and a magnetron sputter source for thin films. The particle density was low and the particles were small. With a higher particle density in the order of a 100 particles per square micron and particles with a diameter of 20-30 nm the effect on the optical properties will be much larger and this makes it easier to observe. Large particles are also easier to detect using AFM, reducing the uncertainty in the particle density. We have made one sample with such particle densities: CS533 had a density of 60 particles per square micron and a typical particle diameter of 20 to 30 nm. Unfortunately we were unable to reproduce these kinds of densities, but the NC-200 cluster source at least has the potential to produce these kinds of particles under ideal circumstances.

A slower deposition of amorphous silicon may also decrease the number of large (4-8) nm features on the surface of the layer, making it easier to detect the nanoparticles and decreasing the uncertainty in the particle density. For silicon nitride the depositions should be done on quartz because effects are observed around 350 nm where glass is already slightly absorbing.

Other techniques such as electron beam lithography[23] or evaporation through a mask can also be used to create this system of aluminium nanoparticles embedded in silicon nitride or amorphous silicon. If the particles are taken out of vacuum, a 2-5 nm oxide layer forms which reduces the size of the metallic core. If large (20-30 nm) particles are used this is no problem. The aluminium oxide layer creates a slight redshift of the resonance[24]. For any potential application towards light trapping in thin film solar cells the scattering must be large compared to the absorption so particles must be large anyway and it is not absolutely necessary to work in high vacuum if only a small oxide layer is formed around the particles.

These systems of aluminium nanoparticles embedded in a dielectric merit more study, especially the system of aluminium nanoparticles embedded in amorphous silicon. Because we expect the dipole resonance to be well-matched to the solar spectrum, although we did not observe an enhancement of the absorption with particles embedded in amorphous silicon. Also, if the higher order modes of plasmonic metal particles are more suited to enhance optical absorption it would be interesting to investigate if the wavelengths of these resonances can be controlled by adjusting the particle shape and size or by embedding the particle in a dielectric.

Acknowledgements (7)

I want to thank Veronique Gevaerts, Maarten Dorenkamper and Klaas Bakker of ECN for their assistance with the DEKTAK, Raman and UV-Vis measurements respectively. Da Wang helped me with the TEM measurements. I want to thank Winjongh Tang for helping me with the AFM measurements and the Zeester vacuum system.

Marcel di Vece was my direct supervisor and I want to thank him for introducing me to a new field, teaching me how to work with the vacuum system, keeping the project on track and being available to answer any question anytime.

[23] (Villesen, 2012)

[24] (Akimov&Koh, Design of Plasmonic Nanoparticles for efficient subwavelength light trapping in thin film solar cells, 2011)

References

Akimov&Koh. (2010). Resonant and nonresonant plasmonic nanoparticle enhancement for thin-film solar cells. *Nanotechnology*.

Akimov&Koh. (2011). Design of Plasmonic Nanoparticles for efficient subwavelength light trapping in thin film solar cells. *Plasmonics*, 155-161.

Akimov, K. (2009). Enhancement of optical absorption in thin film solar cells through the excitation of higher order nanoparticle plasmon modes . *Optical Society of America*, 10196-10205.

Akimov, K. R. (2010). Nanoparticle-enhanced thin film solar cells: Metallic or dielectric nanoparticles? *Applied Physics Letters*, 073111.

al, V. e. (2012). Aluminium nanoparticles for plamon improved coupling of light into silicon. *Nanotechnology*.

al, V. e. (2012). Aluminum nanoparticles for plasmon-improved coupling of light into silicon. *Nanotechnology*.

al., A. D. (1998). Optical properties of metallic films for vertical-cavity optoelectronic devices. *Applied optics*, 5271-5283 .

Ashcroft, N. (1976). *Solid State Physics.* Philadelphia: Holt, Rhineardt & Winston.

Aspnes&Theeten. (1979). Dielectric function of SiSiO2 and SiSi3N4 mixtures. *Journal of Applied Physics*, 4928-4935.

Atwater&Polman. (2013). Plamonics for improved photovoltaic devices. *Nature Materials*, 205-213.

Beck, P. C. (2009). Tunable light trapping for solar cells using localized surface plasmons. *Journal of Applied Physics*, 114310.

Blaber. (2007). Plasmon absorption in nanospheres: a comparison of sodium, potassium, aluminium silver and gold. *Physica B*, 184-187.

de Waele, K. P. (2007). Tunable Nanoscale Localization of Energy on Plasmon Particle Arrays. *Nano Letters*, 2004-2008.

Deshpande, G. B. (1995). Optical properties of silicon nitride films deposited by hot filament CVD. *Journal of Applied Physics*.

First and second-order Raman scattering in Si nanostructures within Silicon Nitride. (2010). *Applied Physics Letters*, 153112.

Hägglund, Z. P. (2008). Electromagnetic coupling of light into a silicon solar cell by nanodisk plasmons . *Applied Physics Letters*, 053110.

Kreibig&Vollmer. (1995). *Optical properties of metal clusters.* Heidelberg: Springer-Verlag.

Lamprecht. (2000). Metal nanoparticle gratings: influence of dipolar particle interaction on the Plasmon resonance. *Physical review letters*, 4721-4724.

Maier, S. (2007). *Plasmonics: Fundamentals and Applications.* Bath: Springer.

Malinovsky. (2000). Investigation of Amorphous states of SiO2 by Raman scattering spectroscopy. *Physics of the Solid state*, 62-68.

Mercaldo. (2010). First and second-order Raman scattering in Si nanostructures within silicon nitride. *Applied Physics letters*, 153112.

Mertens, V. P. (2004). Infrared surface plasmons in two-dimensional silver nanoparticle arrays in silicon. *Applied Physics Letters*, 1317-1319.

Mulvaney, C. &. (2001). Electro-optical shifts in silver nanoparticle films. *Chemical Physics Letters*, 358-362.

Nakayama, T. A. (2008). Plasmonic nanoparticle enhanced light absorption in GaAs solar cells. *Applied Physics Letters*.

nanoparticles?, N.-e. t. (2010). Akimov, Koh, Sian,Ren. *Applied Physics Letters*, 073111.

Philipp, H. R. (1973). Optical Properties of silicon nitride. *Electrochemical Society*, 295-300.

R.Smith, R. a. (n.d.). Magnetron-Based Nanocluster Source: Capabilities, Limitations and Future Possibilities.

Rakić, A. D. (1998). Optical properties of metallic films for vertical-cavity optoelectronic devices. *Applied optics*, 5271-5283.

Rantzer, A. e. (2001). Optical properties of intrinsic and doped a-Si:H films grown by dc magnetron sputter deposition. *Thin Solid Films*, 256-263.

Rouhani, S. (1973). Influence of the surface charge on the metal surface energy. *Surface Science*, 499-502.

Tan, Z. Z. (2014). Plasmonic Color Palettes for Photorealistic Printing with Aluminum Nanostructures. *Nano Letters*.

Turan, G. &. (2010). Effect of particle properties and light polarization on the plasmonic resonances in metallic nanoparticles. *Optical society of America*, 17322-17338.

Verikios, I. &. (1996). Charge transfer in metal catalysts supported on doped TiO2: a theoretical approach based on metal-semiconductor contact theory. *Journal of Catalysis*, 560-569.

Villesen, U. (2012). Aluminum nanoparticles for plasmon-improved coupling of light into silicon. *Nanotechnology*.

Vollmer, K. &. (1995). *Optical properties of Metal Clusters.* Springer Materials Science.

Xu&Ching. (1995). Electronic structure and optical properties of a and P phases of silicon nitride, silicon oxynitride and with comparison to silicon dioxide. *Physical Review B*, 379-388.

Xu, T. N. (2003). Wavelength tuning of surface plasmon resonance using dielectric layers. *Applied Physics Letters*, 3811-3813.

Zhao, K. S. (2003). The Extinction Spectra of Silver Nanoparticle Arrays: Influence of Array Structure on Plasmon resonance wavelength and width. *Journal Of Physical Chemistry*, 7343-7350.

Zhaoping. (1984). Raman and infrared spectra of chlorinated and hydrogenated amorphous silicon. *Chinese Journal of Semiconductors*, 478-483.

Zhdanov. (2002). nm-sized metal particles on a semiconductor surface,. *Surface Science Letters*, 331-334.